

SMA-COATED ALUMINUM STRUCTURAL ELEMENTS WITH ENHANCED-THERMO-MECHANICAL PERFORMANCE

D.A. Exarchos¹, P.T. Dalla¹, I.K. Tragazikis¹, K.G. Dassios¹, C. De Crescenzo², D. Karatza²,
D. Musmarra², S. Chianese², T.E. Matikas¹

¹ Department of Materials Science and Engineering, University of Ioannina, 45110 Ioannina, Greece

² Department of Civil and Building Engineering, Design and Environment, University of Campania "L. Vanvitelli",
81031 Aversa (CE), Italy

ABSTRACT

This work presents the development of novel multifunctional Shape Memory Alloy (SMA) coatings aiming to improve the mechanical behavior of structural components, as well as their corrosion resistance. The groundbreaking concept of the new coating material is described briefly as follows: Upon heating, the SMA coating tends to recover its experienced deformation and return to its original shape. At that point, shear forces developing at the interface between coating and structure are expected to mitigate the deformation of the structure and reduce its overall stress field level. The latter is a great benefit for regions where cracks exist, since the local reduction of the stress field will delay the crack propagation and hence the structural failure.

Numerical analysis is performed to gain understanding of the expected thermomechanical response of the entire SMA-coated composite structure. The influence of the alloy composition and precipitates on the thermomechanical properties are also examined. The SMA coating is subjected to appropriate processing conditions and deposited on metallic substrates of proper geometry following a custom-designed two-phase process, which enables beneficial shape recovery enabling the efficient mitigation of the structure's deformation. Processing consists of aging heat treatments, which are of paramount importance for endowing the coating with the shape memory effect. The effect of heat treatment conditions on the thermo-mechanical fatigue response of the material was also characterized. The developed SMA coatings on aluminum structural elements can find significant application in aeronautical engineering, as for example in the aircraft wing box structure reinforcement and the fuselage structure to enhance their structural integrity.

Key words: Shape memory alloys (SMAs), Coating, Ni-Ti, SMA-coated aluminum, Shape memory effect (SME), Thermomechanical actuation

1. INTRODUCTION

The unique and closely related properties of shape memory and pseudoelasticity, or superelasticity, in SMAs result from a reversible, diffusionless solid-to-solid transformation from austenite to martensite and vice versa under applied mechanical load and/or temperature variations [1-4]. The parent austenite phase transforms to the martensite phase upon cooling, which is dependent on alloy composition, material processing, and stress levels [5]. In the absence of mechanical load, the variants of the low-symmetry martensite phase are usually arranged via twinning in self-accommodation, leading to no obvious macroscopic change in shape. Contrary, under sufficient mechanical loading, only favorably oriented martensite variants form leading to large macroscopic inelastic strains [6]. During heating, martensitic phase reverse transforms back to austenitic phase and the inelastic strains are recovered, a phenomenon shown as shape memory effect [6]. If a mechanical load is applied to the material in the twinned martensitic phase, detwinning is possible by reorientation of a certain number of

variants [6]. The high inelastic strains associated to detwinning are not recovered upon removal of the load, while plastic deformation can take place upon continued loading [6]. Pseudoelasticity involves stress-induced transformation from austenite to detwinned martensite, followed by strain recovery (and concomitant phase transformation back to the parent austenite phase) upon unloading [6]. Beyond the initial loading plateau corresponding to martensitic transformation, the material's deformation response is similar to that of a conventional alloy [6, 7].

Although a plethora of SMA-related work exists in the literature, never has the shape recovery characteristic of such alloys been utilized in coating applications with the purpose of relaxing the deformations experienced by underlying metallic structures, hence improving their structural integrity. This is the objective of the present work wherein an innovative technology is presented for increasing the stiffness and rigidity of such structures while allowing them to withstand expected loading conditions safely, for enhancing the integrity of damaged structures and for protecting them from corrosion.

In this work, a thermomechanical SMA model was initially established and implemented and numerical analysis of the SMA coating and of the SMA coating-structure system was performed to gain insight into their expected thermomechanical response. For this purpose, the unified constitutive model for polycrystalline SMAs proposed by Boyd and Lagoudas [8] was implemented into ABAQUS suite via a user material subroutine. The model was established based on continuum thermodynamics adopting the classical small-strain rate-independent flow theory for equations of evolution of transformation strain [9]. In addition, the driving force for crack propagation at the SMA coating / elastic structure interface was examined.

The SMA material of choice is binary NiTi since this material system exhibits strong shape memory effect and pseudoelastic behavior combined with excellent deformation behavior, high fatigue resistance and resistance to corrosion. Moreover, the crystallography and thermomechanical response of the particular material system are well understood, as are the effects of heat treatment and the variation of transformation temperatures with changes in composition. In addition, NiTi alloys are advantageous over conventional alloys with respect to corrosion resistance since they do not require mixing with other compounds, such as in the case of corrosion-prone alloys (e.g. ferrous alloys) where mixing with copper would offer the desirable anti-corrosive characteristic. Additionally, introduction of precipitates in the microstructure through appropriate heat treatment enables tailoring of the phase transformation temperatures of the NiTi SMAs. Precipitates are non-transforming compounds, which shift the phase transformation temperatures, decrease the phase transformation strain, and suppress the Transformation Induced Plasticity (TRIP) [10-18]. SMAs with two different NiTi compositions are considered, namely equiatomic and Ni_{50.8}Ti_{49.2} (at.%) alloys. While NiTi in equiatomic composition does not form precipitates when heat treated, Ni-rich alloys such as Ni_{50.8}Ti_{49.2} (at.%) SMA form Ni₄Ti₃ precipitates when aged [19]; the precipitates grow in size with raising temperature and heating duration. Ni₄Ti₃ nano-precipitates start to form alongside grain boundaries at smaller aging heat treatment temperatures and durations. Higher aging temperatures or durations lead to the growth of the size of precipitates which start to spread homogeneously across the matrix. With further aging, in terms of either temperature or time, the precipitates continue to grow in size leading coherent precipitates to mix with larger in size incoherent precipitates. Therefore, raising ag-

ing temperature and duration causes evenly distributed, fine, coherent with the matrix precipitates to form large in size incoherent precipitates. Because Ni₄Ti₃ particulates are rich in nickel, their precipitation reduces the nickel in the matrix and therefore makes the matrix richer in titanium in comparison to the original (without precipitates) material. This strengthens the SMA and rises the transformation temperatures because the nickel content in the matrix decreases [20]. In addition, Ni₄Ti₃ precipitates play an important role in the two-way shape memory effect (SME) [21].

Since the objective of this research is to develop NiTi SMA coatings for structural applications, the durability and reliability of bulk SMAs in the desired composition and heat treating conditions are established in order to successfully develop the coating materials under similar conditions. Key to determining the reliability of SMAs is understanding the effect of repeated transformation on the thermomechanical (actuation) response. While many studies have been performed dealing with structural fatigue of SMAs that undergo pseudoelastic cycling in constant temperature, only a few studies have focused on thermal cycling [22-24].

2. THERMOMECHANICAL SMA CONSTITUTIVE MODEL

In the context of elastic isotropic response, increments of the components of strain tensor, $d\varepsilon_{ij}$ are given as

$$d\varepsilon_{ij} = S_{ijkl} d\sigma_{kl} + dS_{ijkl} \sigma_{kl} + d\varepsilon_{ij}^t, \quad (1)$$

where σ_{ij} , ε_{ij}^t are the Cartesian components of the stress tensor and of the transformation strain tensor, respectively, and S_{ijkl} are the components of the current tensor of compliance [25]. The transformation strains are an order of magnitude higher than the thermoelastic strains, therefore the latter can be considered negligible. In this report, standard Einstein notation is utilized and summation over recurrent indices is implicit [26]. The current tensor of compliance changes with the martensitic volume fraction ζ as $S_{ijkl} = (1-\zeta)S_{ijkl}^A + \zeta S_{ijkl}^M$ with S_{ijkl}^A and S_{ijkl}^M the components of the tensor of compliance of the austenitic and martensitic phases. Assuming elastic isotropy for both the austenitic and martensitic phases is

$$S_{ijkl}^\alpha = \frac{1+\nu_\alpha}{2E_\alpha} (\delta_{ii}\delta_{jk} + \delta_{ik}\delta_{jl}) - \frac{\nu_\alpha}{E_\alpha} \delta_{ij}\delta_{kl},$$

where the index α stands for A in the case of austenite and for M in the case of martensite. E_α , ν_α denote the Young's modulus and Poisson's ratio of the two

phases, respectively, and δ_{ij} is Kronecker's delta [27].

An equation of evolution of the transformation strain is defined based on its relation to the martensitic volume fraction evolution ξ ,

$$d\varepsilon_{ij}^t = \Lambda_{ij} d\xi, \quad \Lambda_{ij} = \begin{cases} \Lambda_{ij}^f, & d\xi > 0 \\ \Lambda_{ij}^r, & d\xi < 0 \end{cases} \quad (2)$$

where, Λ_{ij} , the components of the direction tensor, are defined as

$$\Lambda_{ij}^f = \frac{3}{2} \frac{H^{cur}}{\bar{\sigma}} s_{ij}, \quad \Lambda_{ij}^r = \frac{\varepsilon_{ij}^t}{\xi} \quad (3)$$

Where, H^{cur} is the uniaxial transformation strain magnitude for the complete transformation,

$\bar{\sigma} = \sqrt{\frac{3}{2} s_{ij} s_{ij}}$ is the Mises equivalent stress and $s_{ij} = \sigma_{ij} - \sigma_{kk} \delta_{ij} / 3$ are the stress deviator constituents. During forward phase transformation, the transformation strain is oriented in the direction of deviatoric stress, motivating the selected J_2 form of the tensor of direction [27]. During the reverse transformation, it is presumed that the magnitude and direction of the recovery transformation strain is dictated by the mean orientation of martensitic phase at the reversal transformation, which is the endpoint of the forward transformation, partial or full [28]. Such a definition permits the return to zero transformation of strain for each state having insignificant martensitic volume fraction. H^{cur} is a function of the state of stresses since most of SMAs do not show a constant maximum achievable transformation strain at every stress level [29]. The saturated value of the maximum possible transformation strain, H_{sat} , is achieved at high levels of stress, depending on the SMA type as well as on the processing conditions of the polycrystalline material [29]. This, for example, results in different morphological and crystallographic textures. This observation leads to the conclusion that the maximum transformation strain H^{cur} can be described by the following decaying exponential function

$$H^{cur}(\bar{\sigma}) = H_{sat} (1 - e^{-k\bar{\sigma}}) \quad (4)$$

where the parameter k controls the rate at which H^{cur} exponentially evolves from 0 to H_{sat} . During the transformation, the components of stress tensor must stay on the transformation surface

$$\Phi = 0, \quad \Phi = \begin{cases} \Phi^f = \pi^f - Y, & d\xi > 0 \\ \Phi^r = -\pi^r - Y, & d\xi < 0 \end{cases} \quad (5)$$

Where π^f and π^r are the thermodynamic driving forces for the forward and reverse phase transformations and Y is the thermodynamic force critical value for starting and withstanding the phase transformations (forward and reverse). The thermodynamic driving force for forward transformation is written as

$$\pi^f = \sigma_{ij} \Lambda_{ij}^f + \frac{1}{2} \Delta S_{ijkl} \sigma_{ij} \sigma_{kl} + \rho \Delta s_0 T - \rho \Delta u_0 - f^f \quad (6)$$

where

$$f^f = \frac{1}{2} \alpha_1 [1 + \xi^{n_1} - (1 - \xi)^{n_2}] + \alpha_3 \quad (7)$$

and for reverse transformation

$$\pi^r = \sigma_{ij} \Lambda_{ij}^r + \frac{1}{2} \Delta S_{ijkl} \sigma_{ij} \sigma_{kl} + \rho \Delta s_0 T - \rho \Delta u_0 - f^r \quad (8)$$

where

$$f^r = \frac{1}{2} \alpha_2 [1 + \xi^{n_3} - (1 - \xi)^{n_4}] - \alpha_3 \quad (9)$$

f^f and f^r are functions which describe the behavior of transformation hardening throughout the forward and reverse transformations, respectively. s_0 and u_0 are the specific entropy and internal energy, respectively, ρ is the density, Δ denotes the difference in property between the martensitic and the austenitic states, α_i ($i=1,2,3$) and n_i ($i=1,2,3$) are coefficients that assume real number values [27].

3. NUMERICAL IMPLEMENTATION OF THE SHAPE MEMORY ALLOY CONSTITUTIVE MODEL

The developed constitutive model was employed in ABAQUS via a user material subroutine termed UMAT. Voigt notation was used in order to express the necessary equations. The highly non-linear response of SMAs requires the utilization of a non-linear FE analysis procedure. The FE analysis procedure is discretized in a finite number of time steps in order to precisely capture the material response. Additionally, because of the appearance of the time derivatives of the external material state variable and internal material state variable ξ , the analysis is not only non-linear but also transient. Hence, each analysis step corresponds to a physical time step with resolution Δt , each beginning at time t and ending at time $t + \Delta t$. The Newton-Rapson (N-R) iterative-incremental procedure is utilized by the ABAQUS global solver at every time step of the analysis for the solution of the FE problem and an implicit time

integration technique.

In brief, the N-R process in each time step provides a guess of the nodal displacements and temperatures which are the independent variables of the thermo-mechanical equilibrium equations and the solution variables of the problem. Then the aforementioned variables are used to calculate the values of total strain, ε , at the integration points of each FE. Subsequently, the latter variables are passed, for each element, in the UMAT subroutine accompanied by the chosen state variables ξ and ε^t , which are also referring to the integration points of the FE and account for material's loading path history dependence. In the UMAT subroutine, the stress is calculated along with its partial derivative with respect to the independent variable ε . Finally, the values of the state variables are updated and passed to the ABAQUS global solver along with all the aforementioned terms. The value of stress is used for the calculation of the element nodal forces whereas its partial derivative is used for the calculation of the tangential matrix which is required by the N-R procedure. The forces from all neighboring elements, that act at the coincident nodes, are added and the total force at any particular node equals null in order to fulfill the requirement of equilibrium. If the magnitude of the residual vector (vector of the sums) is adequately small, the total solution is deemed to be precise and the next time-step starts. If the magnitude is too large, N-R computes a new guess for the solution variables and the process is repeated until the residuals become smaller than a predefined limit.

3.1 Time Discretized Constitutive Equations

Provided that the analysis procedure is partitioned into time steps, throughout the rest of this discussion the values of the terms referred to the beginning of each time step will be denoted with the superscript t while at the end of the time increment with the superscript $t+\Delta t$. In order to discretize in time, a backwards finite difference formula is utilized, via

$$\dot{X}_{t+\Delta t} = \frac{X_{t+\Delta t} - X_t}{\Delta t}, \quad (10)$$

where, X denotes the variables to be differentiated; superscripts denote the respective time step [29]. Thus the evolution equation in its discretized form reads

$$\varepsilon_{t+\Delta t}^t = \varepsilon_t^t + (\xi_{t+\Delta t} - \xi_t) \mathbf{A}_{t+\Delta t} \quad (11)$$

In the same manner, Hooke's law is given in its time discretized form as

$$\sigma_{t+\Delta t}(\varepsilon_{t+\Delta t}, \varepsilon_{t+\Delta t}^t, \xi_{t+\Delta t}) = \mathbf{C}_{t+\Delta t}(\varepsilon_{t+\Delta t} - \varepsilon_{t+\Delta t}^t) \quad (12)$$

along with the Kuhn-Tucker conditions given by

$$\left(\frac{\xi_{t+\Delta t} - \xi_t}{\Delta t} \right) \geq 0, \Phi_{t+\Delta t}^f \leq 0, \Phi_{t+\Delta t}^f \left(\frac{\xi_{t+\Delta t} - \xi_t}{\Delta t} \right) = 0, \quad (13)$$

$$\left(\frac{\xi_{t+\Delta t} - \xi_t}{\Delta t} \right) \leq 0, \Phi_{t+\Delta t}^r \leq 0, \Phi_{t+\Delta t}^r \left(\frac{\xi_{t+\Delta t} - \xi_t}{\Delta t} \right) = 0, \quad (14)$$

where the transformation functions for forward and reverse transformation are [29]

$$\begin{aligned} \Phi_{t+\Delta t}^f(\sigma_{t+\Delta t}, \xi_{t+\Delta t}) &= (\sigma_{t+\Delta t})^T \mathbf{A}_{t+\Delta t}^f \\ &+ \frac{1}{2} (\sigma^T)_{t+\Delta t} \Delta \mathbf{S} \sigma_{t+\Delta t} - \rho \Delta c \left((T - T_0) - T \ln \frac{T}{T_0} \right) \\ &+ \rho \Delta s_0 T - \rho \Delta v_0 - (f_t^f)_{t+\Delta t} - Y \end{aligned} \quad (15)$$

and

$$\begin{aligned} \Phi_{t+\Delta t}^r(\sigma_{t+\Delta t}, \xi_{t+\Delta t}) &= -(\sigma_{t+\Delta t})^T \mathbf{A}_{t+\Delta t}^r \\ &- \frac{1}{2} (\sigma^T)_{t+\Delta t} \Delta \mathbf{S} \sigma_{t+\Delta t} + \rho \Delta c \left((T - T_0) - T \ln \frac{T}{T_0} \right) \\ &- \rho \Delta s_0 T + \rho \Delta v_0 + (f_t^r)_{t+\Delta t} - Y. \end{aligned} \quad (16)$$

Given the time-discretized form of the preceding equation and the aforementioned clarifications, the description of the algorithm can follow.

3.2 Thermo-Elastic Prediction

At the beginning of each time step the value of $\varepsilon_{t+\Delta t}$ is known based on the guesses of the N-R process regarding the solution variables and are input to UMAT subroutine as follows

$$\varepsilon_{t+\Delta t} = \varepsilon_t + \Delta \varepsilon \quad (17)$$

where $\Delta \varepsilon$ is the increment of the respective variable in the current time step. In the same manner the chosen state variables are provided as input to the UMAT and are considered equal to their value on the last converged time step

$$\xi_{t+\Delta t} = \xi_t \quad (18)$$

$$\varepsilon_{t+\Delta t}^t = \varepsilon_t^t \quad (19)$$

It is worth pointing out that if the previous step is the initial step, the values of ε_t , ξ_t and ε_t^t depict the initial conditions of the problem. At this point the thermo-elastic prediction step begins; this is a trial step with a scope to verify whether the trial values of state variables comply with the time discrete Kuhn-Tucker conditions. To this end, the current stress value is calculated given the value of $\varepsilon_{t+\Delta t}$ and the assumptions regarding $\xi_{t+\Delta t}$ and $\varepsilon_{t+\Delta t}^t$. If $\Phi_{t+\Delta t}^f < 0$ and $\Phi_{t+\Delta t}^r < 0$, the Kuhn-Tucker conditions indicate that no transformation takes place. Hence, the

trial values of $\xi_{t+\Delta t}^z$ and $\varepsilon_{t+\Delta t}^t$ are considered correct and the algorithm proceeds to the following step of the algorithm. On the other hand, if $\Phi_{t+\Delta t}^r$ or $\Phi_{t+\Delta t}^r$ have a positive value the Kuhn-Tucker conditions of the corresponding forward or reverse transformation are violated, meaning that the trial state lies outside the transformation surface and in order to return on the transformation surface the closest point projection return mapping algorithm is used.

3.3 Return Mapping Algorithm

The return mapping algorithm is an iterative process which aims to calculate the correct values of $\xi_{t+\Delta t}^z$ and $\varepsilon_{t+\Delta t}^t$ for given values of $\varepsilon_{t+\Delta t}$ in order for the thermo-mechanical state to return on the transformation surface. A N-R solution method is thus employed for the solution of the following system of equations [29]

$$\mathbf{R}_{t+\Delta t}^{(\kappa)}(\sigma_{t+\Delta t}, \varepsilon_{t+\Delta t}^t, \xi_{t+\Delta t}^z) = -\varepsilon_{t+\Delta t}^{(\kappa)} + \varepsilon_t^t + (\xi_{t+\Delta t}^z - \xi_t^z) \mathbf{\Lambda}_{t+\Delta t}^{(\kappa)} = 0, \quad (20)$$

$$\Phi_{t+\Delta t}^{(\kappa)}(\sigma_{t+\Delta t}, \xi_{t+\Delta t}^z) = 0, \quad (21)$$

where the subscript, κ , indicates the k^{th} iteration of the N-R process and \mathbf{R}^r is the transformation strain residual. In order to solve the system of equations, the expression of $\sigma_{t+\Delta t}$ is substituted in both equations and transforms them to functions of variables $\varepsilon_{t+\Delta t}^t$, $\varepsilon_{t+\Delta t}^t$ and $\xi_{t+\Delta t}^z$. Finally taking into account that the values of $\varepsilon_{t+\Delta t}$ are given by the N-R iterative-incremental procedure of ABAQUS global solver, the aforementioned equations become functions of variables $\varepsilon_{t+\Delta t}^t$ and $\xi_{t+\Delta t}^z$ only. During the initiation of the N-R process, the trial values of $\xi_{t+\Delta t}^z$, $\varepsilon_{t+\Delta t}^t$ provided by the thermo-elastic prediction step as per

$$\xi_{t+\Delta t}^{(0)} = \xi_{t+\Delta t}^z, \quad (22)$$

$$\varepsilon_{t+\Delta t}^{(0)} = \varepsilon_{t+\Delta t}^t, \quad (23)$$

are used as initial conditions of the N-R process, which is defined as

$$-\begin{bmatrix} \frac{\partial \mathbf{R}_{t+\Delta t}^{(k)}}{\partial \varepsilon_{t+\Delta t}^t} & \frac{\partial \mathbf{R}_{t+\Delta t}^{(k)}}{\partial \xi_{t+\Delta t}^z} \\ \frac{\partial \Phi_{t+\Delta t}^{(k)}}{\partial \varepsilon_{t+\Delta t}^t} & \frac{\partial \Phi_{t+\Delta t}^{(k)}}{\partial \xi_{t+\Delta t}^z} \end{bmatrix} \begin{bmatrix} \Delta \varepsilon_{t+\Delta t}^t \\ \Delta \xi_{t+\Delta t}^z \end{bmatrix} = \begin{bmatrix} \mathbf{R}_{t+\Delta t}^{(k)} \\ \Phi_{t+\Delta t}^{(k)} \end{bmatrix} \quad (24)$$

The linearized system of the above equations is solved for $[\Delta \varepsilon_{t+\Delta t}^t \Delta \xi_{t+\Delta t}^z]^T$ and a new guess of the solution variables,

$$\begin{bmatrix} \varepsilon_{t+\Delta t}^{(k+1)} \\ \xi_{t+\Delta t}^{(k+1)} \end{bmatrix} = \begin{bmatrix} \varepsilon_{t+\Delta t}^{(k)} \\ \xi_{t+\Delta t}^{(k)} \end{bmatrix} + \begin{bmatrix} \Delta \varepsilon_{t+\Delta t}^t \\ \Delta \xi_{t+\Delta t}^z \end{bmatrix}, \quad (25)$$

is calculated. The iterations repeated until the residual load vector $\begin{bmatrix} \mathbf{R}_{t+\Delta t}^{(k)} \\ \Phi_{t+\Delta t}^{(k)} \end{bmatrix}$ converges to zero values. The convergence of the N-R process leads to the correct values of $\xi_{t+\Delta t}^z$, $\varepsilon_{t+\Delta t}^t$ under the given conditions of $\varepsilon_{t+\Delta t}$ and marks the initiation of the next step of the algorithm.

During this final step of the algorithm, the N-R process adopted by the FE code requires the values of $\frac{\partial \sigma_{t+\Delta t}}{\partial \varepsilon_{t+\Delta t}}$

in order to calculate the FE tangent stiffness matrix. Its calculation using the continuum corresponding equations instead of the time-discretized ones is not providing quadratic convergence rate in the FE N-R process and is conditionally stable. The consistent approach to achieve quadratic convergence rate in the N-R process implies that the time-discretized expressions of the aforementioned equations should be used and this approach is adopted.

The expression of the required partial derivative can be acquired by calculating the differential form of $\sigma_{t+\Delta t}$ as [29]

$$d\sigma_{t+\Delta t} = \frac{\partial \sigma_{t+\Delta t}}{\partial \varepsilon_{t+\Delta t}} d\varepsilon_{t+\Delta t}. \quad (26)$$

The following two cases should be considered.

Partial derivative calculation during thermo-elastic step.– In case of no transformation occurrence, $\varepsilon_{t+\Delta t}^t$ and $\xi_{t+\Delta t}^z$ are considered as constants and $\sigma_{t+\Delta t}$ becomes a function of independent variable $\varepsilon_{t+\Delta t}$. The differential form of $\sigma_{t+\Delta t}$ can thus be trivially acquired as

$$d\sigma_{t+\Delta t} = \mathbf{C}_{t+\Delta t} d\varepsilon_{t+\Delta t} \quad (27)$$

and the needed partial derivative as

$$\frac{\partial \sigma_{t+\Delta t}}{\partial \varepsilon_{t+\Delta t}} = \mathbf{C}_{t+\Delta t}. \quad (28)$$

Partial derivative calculation during transformations.– In case of transformation occurrence, the differential form of $\sigma_{t+\Delta t}$ is calculated using equation [29]

$$d\varepsilon_{t+\Delta t} = \left(\mathbf{S}_{t+\Delta t} + \frac{\partial \mathbf{\Lambda}_{t+\Delta t}}{\partial \sigma_{t+\Delta t}} (\xi_{t+\Delta t}^z - \xi_t^z) \right) \quad (29)$$

$$d\sigma_{t+\Delta t} + d\xi_{t+\Delta t}^z (\Delta \mathbf{S} \sigma_{t+\Delta t} + \mathbf{\Lambda}_{t+\Delta t}),$$

which yields after trivial numerical manipulations the following expression of the partial derivative

$$\frac{\partial \sigma_{t+\Delta t}}{\partial \varepsilon_{t+\Delta t}} = \left[\mathbf{A}_{t+\Delta t}^1 - \mathbf{A}_{t+\Delta t}^2 \frac{\left(\frac{\partial \Phi_{t+\Delta t}}{\partial \sigma_{t+\Delta t}} \right)}{\left(\frac{\partial \Phi_{t+\Delta t}}{\partial \xi_{t+\Delta t}^z} \right)} \right]^{-1}. \quad (30)$$

where

$$\mathbf{A}_{t+\Delta t}^1 = \mathbf{S}_{t+\Delta t} + \frac{\partial \mathbf{\Lambda}_{t+\Delta t}}{\partial \boldsymbol{\sigma}_{t+\Delta t}} (\boldsymbol{\xi}_{t+\Delta t} - \boldsymbol{\xi}_t), \quad (31)$$

and

$$\mathbf{A}_{t+\Delta t}^2 = \Delta \mathbf{S} \boldsymbol{\sigma}_{t+\Delta t} + \mathbf{\Lambda}_{t+\Delta t}. \quad (32)$$

4. NUMERICAL ANALYSIS OF THE SMA COATING

In order to assess the effectiveness of the implemented constitutive law, numerical simulations of the shape memory effect are compared against experimental data obtained from NiTi wires that have been exposed to thermal sweeps under isobaric conditions of loading. To this end, the material parameters need to be calibrated from experimental data. The calibration process of the model parameters is presented below while the comparison between experiments and simulations follows in the next section.

The experimental response of the material under uniaxial loading is mathematically sufficient for calibration. Thus, the model (the set of needed constitutive equations) is first reduced to a form sufficient to describe a 1-D stress state (i.e. $\boldsymbol{\sigma} \rightarrow \sigma_{11} = \sigma$, $\boldsymbol{\varepsilon} \rightarrow \varepsilon_{11} = \varepsilon$ etc.) [29].

The relation between the current stress and strain reduces to

$$\sigma = E(\xi) [\varepsilon - \varepsilon^t], \quad (33)$$

where the current E is defined as

$$E(\xi) = [1/E^A + \xi(1/E^M - 1/E^A)]^{-1}. \quad (34)$$

The evolution equation for the transformation strain reduces to

$$\dot{\varepsilon}^t = \dot{\xi} \Lambda^t; \quad \Lambda^t = \begin{cases} H^{cur}(\sigma) \text{sgn}(\sigma); & \dot{\xi} > 0, \\ \varepsilon^t / \xi; & \dot{\xi} < 0. \end{cases} \quad (35)$$

Ignoring the effects of Δc (a usual engineering assumption), the transformation function during forward transformation is given as

$$\Phi^f(\sigma, T, \xi) = |\sigma| H^{cur}(\sigma) + \frac{1}{2} \left(\frac{1}{E^M} - \frac{1}{E^A} \right) \quad (36)$$

$$\sigma^2 + \rho \Delta s_0 T - \rho \Delta u_0 - f^f(\xi) - Y = 0,$$

while for reverse transformation it can be written as

$$\Phi^r(\sigma, T, \xi) = -\sigma \frac{\varepsilon^t}{\xi} - \frac{1}{2} \left(\frac{1}{E^M} - \frac{1}{E^A} \right) \quad (37)$$

$$\sigma^2 - \rho \Delta s_0 T + \rho \Delta u_0 + f^r(\xi) - Y = 0.$$

Given those constitutive equations, the model pa-

rameters requiring calibration are: (a) the elastic parameters of the martensitic and austenitic phase, (b) the parameters included in the maximum transformation strain functional form $H^{cur}(\boldsymbol{\sigma})$, and (c) the model parameters ($\rho \Delta s_0$, $\rho \Delta u_0$, α_1 , α_2 , α_3 , Y) which characterize the martensite transformation.

The common material properties that are used to calibrate the model are E_A , E_M , V_A , V_M , H_{sa} , M_s , M_f , A_s , A_f , C_M and C_A . M_s , M_f , A_s and A_f are the martensite start, martensite end, austenite start and austenite end temperatures at null load condition, respectively, and C_M , C_A are the transformation slopes, forward and reverse, in stress-temperature phase diagram (Fig.1) [9]. The constants of elasticity may be directly computed from stress-strain curves (isothermal), where the loading is applied at temperature out of the transformation limits. Calibration of the parameters $H^{cur}(\boldsymbol{\sigma})$ is feasible using isobaric testing of the material, and the value of k can be chosen based on the best fit of the experimental curve [9]. The remaining parameters can be calibrated using the conditions for which the forward transformation starts and finishes in the stress-temperature curve [29]. Since there is no material property related to the exponents n_i ($i=1,2,3,4$) these are chosen based on best fitting of the two corners of the forward transformation diagrams.

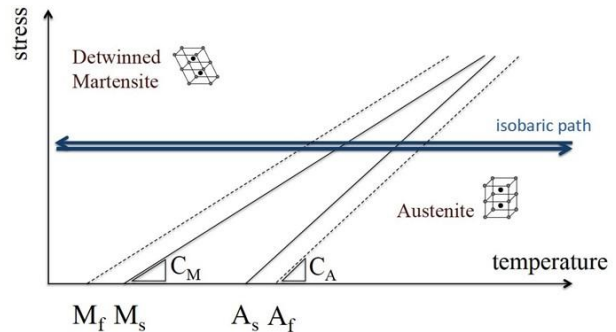


Fig. 1: Stress-temperature phase diagram showing a thermal cycle at constant applied load.

A straightforward method for calibrating these remaining parameters is to first consider transformation occurring under stress-free conditions. Forward transformation ($\dot{\xi} > 0$) at zero stress begins at the martensitic start temperature M_s and ends at M_f . Likewise, reverse transformation ($\dot{\xi} < 0$) at zero stress begins at A_s and ends at A_f . Given these four characteristic temperatures, we can consider the following four states, providing four independent equations [9]:

1. Beginning of forward transformation:
 $\Phi_{fwd}^t(0, M_s, 0) = 0$
2. Ending of forward transformation:
 $\Phi_{fwd}^t(0, M_f, 1) = 0$

3. Beginning of reverse transformation:

$$\Phi'_{rev}(0, A_s, 1) = 0$$

4. Ending of reverse transformation:

$$\Phi'_{rev}(0, A^f, 0) = 0$$

By virtue of the full recovery provided by the martensite transformation in SMAs, the internal and external variables should return to their initial values after the material undergoes a complete transformation cycle [9]. It follows that the material should return to its initial state as the Gibbs free energy returns to its initial value. Thus, a fifth condition is provided [9]:

$$5. \int_0^1 f^f d\xi + \int_1^0 f^r d\xi = 0.$$

Applying these five conditions, we arrive at the following relations for the five model parameters $\rho\Delta u_0$, α_1 , α_2 , α_3 , and [9]:

$$a_1 = \rho\Delta s_0(M^f - M_s), \quad a_2 = \rho\Delta s_0(A_s - A^f),$$

$$a_3 = -\frac{a_1}{4} \left(1 + \frac{1}{n_1 + 1} - \frac{1}{n_2 + 1} \right) + \frac{a_2}{4} \left(1 + \frac{1}{n_3 + 1} - \frac{1}{n_4 + 1} \right), \quad (38)$$

$$\rho\Delta u_0 = \frac{\rho\Delta s_0}{2} (M_s + A^f), \quad Y = \frac{\rho\Delta s_0}{2} (M_s - A^f) - a_3.$$

Calibration of $\rho\Delta s_0$ is performed by considering the slope of the transformation surface in a uniaxial stress-temperature space as measured at a reference stress level, here denoted σ^* . The Kuhn-Tucker conditions imply that the transformation function (and thus its rate of change) are zero-valued during transformation, allowing to write (in 1-D form) [9]

$$d\Phi = \partial_\sigma \Phi d\sigma + \partial_T \Phi dT + \partial_\xi \Phi d\xi = 0. \quad (39)$$

For this calibration, we consider the configuration of the transformation surface at some known constant ξ (usually $\xi=0$ or $\xi=1$), thus $d\xi=0$. Evaluating the remaining partials and solving for the stress-temperature derivatives [9] gives

$$\left. \frac{d\sigma}{dT} \right|_{\sigma=\sigma^*} = \frac{-\rho\Delta s_0}{\Lambda + \sigma \partial_\sigma \Lambda + \sigma \left(\frac{1}{E^M} - \frac{1}{E^A} \right)} \Bigg|_{\sigma=\sigma^*}, \quad (40)$$

which yields

$$C^M = \frac{-\rho\Delta s_0}{\Lambda^f + \sigma \partial_\sigma \Lambda^f + \sigma \left(\frac{1}{E^M} - \frac{1}{E^A} \right)} \Bigg|_{\sigma=\sigma^*, \xi>0} \quad (41)$$

$$= C^A = \frac{-\rho\Delta s_0}{\Lambda^r + \sigma \partial_\sigma \Lambda^r + \sigma \left(\frac{1}{E^M} - \frac{1}{E^A} \right)} \Bigg|_{\sigma=\sigma^*, \xi<0}, \quad (41)$$

and, thus,

$$\rho\Delta s_0 = \frac{-2(C^M)^2 \left[H^{cur}(\sigma) + \sigma \partial_\sigma H^{cur}(\sigma) + \sigma \left(\frac{1}{E^M} - \frac{1}{E^A} \right) \right]}{2C^M} \Bigg|_{\sigma=\sigma^*}. \quad (42)$$

5. NUMERICAL ANALYSIS OF THE SMA-COATING-STRUCTURE

The effectiveness of the implemented constitutive law in the combined SMA coating and underlying structure performance is assessed in this section. Since aircraft structures such as the aircraft wing box structure reinforcement and the fuselage, are modular structures constructed of beams, the feasibility of this research is being demonstrated in a single beam structure. Such SMA coating applications entail, therefore, a long prism of metal with its lateral surfaces encased in SMA coating.

5.1 Modeling the structure: Compressive stresses induced in the elastic structure from the SMA coating

A long rectangular aluminum beam with its lateral surfaces encased in SMA coating is considered (Fig. 2). The dimensions are defined as follows: l_x , l_y , and l_z represent the dimensions of the elastic structure as they correspond to the respective coordinate axes and t_{SMA} represents the thickness of the SMA coating. Note that the SMA coating is encased only on the free surfaces of the beam with perpendicular to the y -direction. L_x and L_z denote $l_x + t_{SMA}$, and $l_z + t_{SMA}$ respectively. For the adopted geometry $l_x=4\text{mm}$, $l_z=4\text{mm}$, $l_y=4\text{mm}$, and $t_{SMA}=0.01\text{mm}$, which yields an SMA coating ratio of 1:400 (the ratio of the thickness of the SMA coating to the smallest dimension of the matrix in the x - z plane). Two more geometries are considered with SMA coating ratios of 1:50 and 1:10. For these geometries, either the longitudinal length and the SMA-coating thickness remain unchanged while the thickness of the elastic structure changes or, equivalently, the longitudinal length and the elastic structure thickness remain unchanged while the SMA-coating thickness changes.

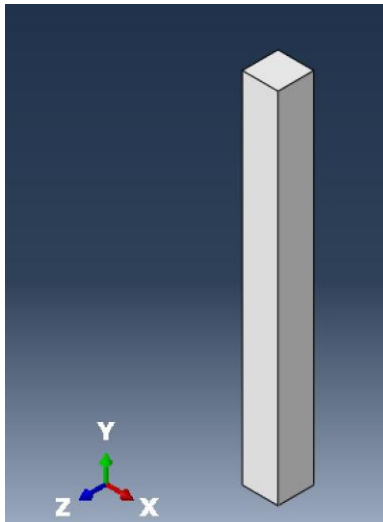


Fig. 2: Basic geometry of SMA coating–structure model.

Two different loading paths are considered in the analysis, namely:

- i. the SMA coating is assumed initially in the austenitic phase and a uniaxial tensile load is applied in the longitudinal direction (y -direction) sufficient for phase transformation from austenite to martensite, followed by a subsequent heating sufficient to induce reverse transformation back to austenite and
- ii. the SMA coating is oriented martensite in the longitudinal direction i.e., there is a macroscopic strain that can be recovered upon heating that will induce phase transformation from martensite to austenite

If the dimensions of the beam are orders of magnitudes greater than the thickness of the SMA coating, which is the case for the geometry at hand -and should be the case in most structural applications involving coatings- then proper discretization using 3-D elements may lead to millions of finite elements, which renders a numerical solution intractable. One way out is the use of shell elements for simulating the SMA coating. Here, a different approach is adopted. Actually, both approaches were tested and found to yield results that differ by less than 2%. Periodic boundary conditions are assumed on a thin (in the y -direction) slice of the structure, such as the one presented in Fig. 3. To further simplify the calculations, only one quarter of the geometry is considered and symmetry conditions are applied. This geometry and boundary conditions approximate the mechanical fields of the original problem away from the boundaries in y -direction ($y=0$, and $y=l_y$) as long as the longitudinal length l_y is a lot bigger than the other dimensions of the structure. The simplic-

ity of the geometry allows imposition of periodic boundary conditions by fixing of the bottom faces of both the aluminum beam and the SMA in the y -direction and by constraining the top faces of both materials to remain planar and parallel to the bottom faces. Rigid body motion is suppressed by pinning the node on the bottom surface of the elastic structure at the center of the full geometry (at the corner of the quarter geometry that is farthest away from the SMA coating), thus constraining the displacement of the node in all three coordinate directions. To apply symmetric boundary conditions, the negative x -faces and negative z -faces of both the matrix and the SMA are constrained with x -symmetry and z -symmetry constraints respectively, thus fixing their displacement along their normal axis and their rotation along their two planar axes.

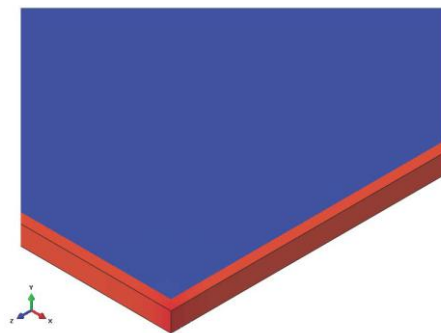


Fig. 3: Basic geometry of SMA coating–structure model representing one quarter of a thin in the y -direction slice of the original structure presented in Fig. 2. The SMA is represented with the red color and the elastic structure with the blue.

The properties of the chosen SMA for the numerical simulations presented here are shown in Table 1 [2] and those of the aluminum beam in Table 2.

For the first loading path, wherein the SMA-coating deforms together with the elastic structure under an applied uniaxial load in the y -direction, the volume ratio between the SMA-coating and the aluminum beam is such that although the temperature at the application of the load is just 3 degrees above the martensitic start temperature M_s the stiffness of the elastic structure requires almost 1.8GPa stress value for the phase transformation in the coating to finish (Fig. 4). The reason being that the transformation strains of the coating should be matched by the elastic deformation of the beam. Subsequent heating of the whole structure reduces the levels of stress in the elastic structure negligibly (Fig. 5). These results are of course dependent on the elastic properties of the two phases however, in any case, the required load

levels for the transformation strain to take values above 0.01 in the SMA coating for this geometry are extremely high for practical applications. Thus, it seems that this loading path cannot be beneficial for the aluminum beam.

Table 1: SMA parameter values.

parameter	value	parameter	value
E_A [GPa]	33	H_{sat}	0.025
E_M [GPa]	15	M^f [K]	227
$\nu_A = \nu_M$	0.33	M_s [K]	242
A_s [K]	261	A^f [K]	270
		C_A [MPa K ⁻¹]	4.5
		C_M [MPa K ⁻¹]	4.5

Table 2: Elastic properties of aluminum

parameter	value
E [GPa]	68.9
ν	0.33

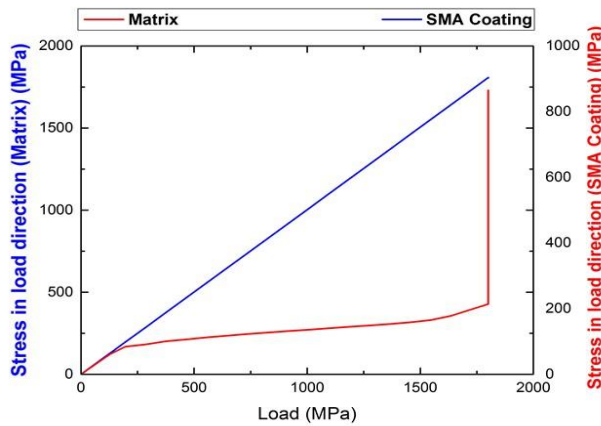


Fig. 4: Normal stress in the longitudinal direction σ_{yy} as a function of applied load.

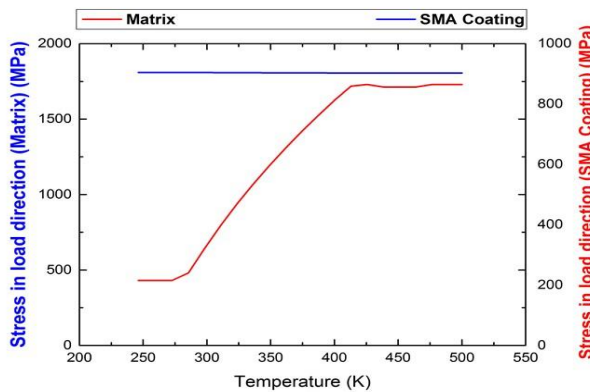


Fig. 5: Normal stress in the longitudinal direction σ_{yy} as a function of temperature (K)

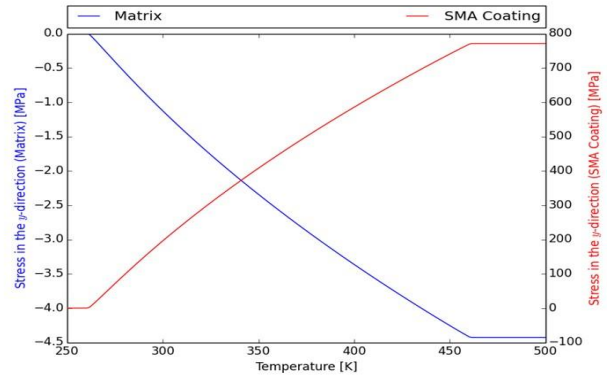


Fig. 6: Normal stress in the longitudinal direction σ_{yy} as a function of temperature (K) for both the matrix and the SMA coating of the 1:400 model

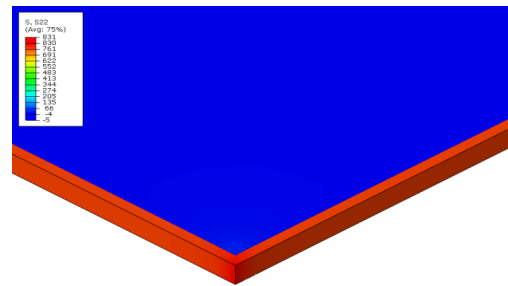


Fig. 7: Enlarged view of normal stress in the longitudinal direction σ_{yy} for the 1:400 model after full transformation

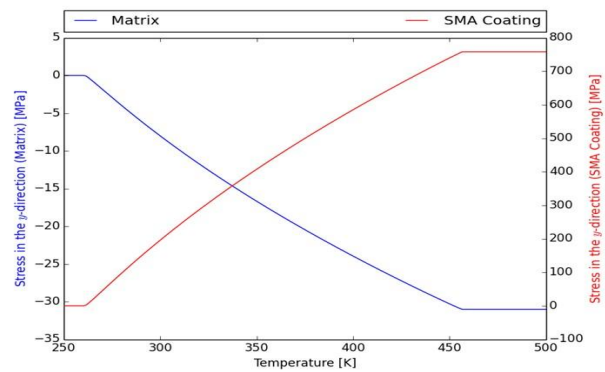


Fig. 8: Normal stress in the longitudinal direction σ_{yy} as a function of temperature (K) for both the matrix and the SMA coating of the 1:50 model

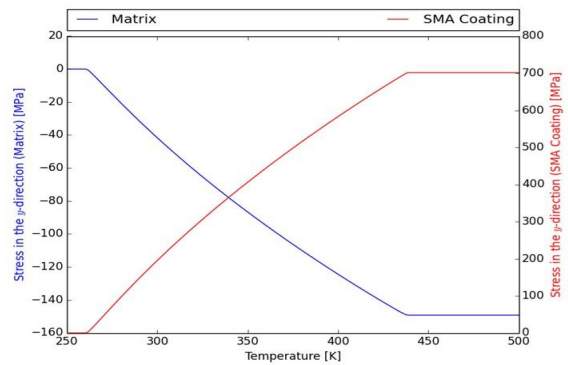


Fig. 9: Stress (MPa) in the loading direction as a function of temperature (K) for both the matrix and the SMA coating of the 1:10 model

An alternative loading path is considered wherein the SMA-coating is assumed to be in an oriented (in the y -direction) martensitic state at zero load and the whole structure is heated for contraction in the coating to take place by reverse phase transformation and compressive stresses to develop in the elastic structure. In Fig. 6, the evolution of the normal component of the stress tensor in the y -direction, i.e., σ_{yy} during heating is presented in both the SMA coating and the elastic structure. Here, stresses are observed to be almost uniform except from a very small region at the interface between the two phases (Fig. 7). The initial strain in the SMA before heating, i.e. in the martensite state, is $\varepsilon_{yy} = 0,025$ and the stress is null both in the SMA and the aluminum beam. During heating and as the SMA starts transforming into austenite recovering its initial deformation, the stress level in the SMA increases (tensile stresses develop) resulting in a compressive stress state in the elastic structure. The increase of stress in the SMA coating shifts the required temperature for further reverse transformation from martensite to austenite (see phase diagram in Fig. 1). The ratio of the thickness of the coating to the smallest dimension of the aluminum beam is such that the experienced tensile stress, once the coating is fully transformed into austenite, reaches as high as 780 MPa. Such stress levels require heating of around 200 K for the initiation to the end of phase transformation. At the end of phase transformation, the compressive stress value in the beam is a low as 4 MPa. These results are expected from a rule of mixtures perspective since the load carrying capacity of the SMA coating in the modeled structure of a ratio 1:400 is quite limited.

Next, the geometry is altered, namely the ratio of the SMA thickness to smallest dimension of the aluminum beam is changed to 1:50 and the levels of compressive stresses that can be developed in the elastic structure are evaluated (Fig. 8). For this geometry, the compressive stresses developed in the beam once the coating is fully transformed to austenite reach approximately 30 MPa while the tensile stress level in the coating is around 750 MPa. As in the previous case, a temperature raise of approximately 200 K is required for full phase transformation. Lastly, for a ratio of 1:10, the compressive stresses developed in the beam once the coating is fully transformed to austenite is approximately 100 MPa while the tensile stress level in the coating is around 700 MPa (Fig. 9). The temperature raise needed for full transformation is around 180 K.

5.2 Driving Force for Crack Growth at the Interface between SMA-Coating and Elastic Structure

For the numerical investigation of the driving force for crack growth at the SMA coating – elastic structure interface, a beam of a circular cross section consisting of an aluminum core of radius r and an SMA coating of thickness $t_{SMA} = 0.01$ mm is considered. An interfacial imperfection between the aluminum and SMA structure is introduced as an initial crack of length t_c as depicted in Fig. 10. The introduction of the initial crack will enable to determine the driving force for decohesion of the SMA-coating and aluminum core during the reverse transformation required to develop the compressive stresses in the aluminum core. Thus, as in the previous section, the SMA coating is considered at an axially pre-strained martensitic phase and it is heated to return to austenite. The resulting loading mode close to the crack tip is mixed, i.e., mode I and II. The models are developed with the continuum 3D FEs (C3D20R) and 3D shell FEs (S4R) of ABAQUS FE software.

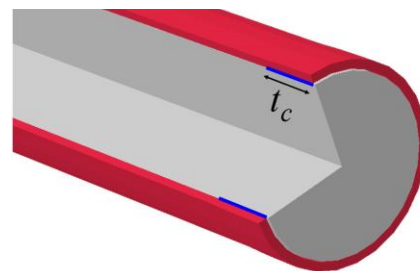


Fig. 10: Aluminum beam with SMA coating with initial crack.

The driving force for crack growth is calculated using the Virtual Crack Closure Technique (VCCT) [9]. This technique is considered advantageous due to its simplicity under mixed mode loading conditions compared to other available techniques such as XFEM or cohesive elements. The latter, for example, requires at least two parameters for defining the cohesive-traction separation law for each fracture mode, instead of one for VCCT, and the choice of these has a great influence on the toughness response of the structure [30]. Thus, in the absence of experimental data on the toughness of the interface, the use of cohesive elements would require an extensive parametric study that would not even be conclusive. The VCCT approach on the other hand yields a single value for the driving force for crack growth, that of the energy release rate (G_I and G_{II} , corresponding to mode I and mode II, respectively), thus giving a straightforward approximation of the required interface toughness for structural integrity

and its use has been moreover justified in the SMA literature [26].

In the case of the axisymmetric eight-noded elements placed in the crack front, the VCCT method yields for G_I , [27]

$$G_I = -\frac{1}{2\Delta a} \left[F_2^i (u_2^l - u_2^{l*}) + F_2^j (u_2^m - u_2^{m*}) \right]$$

where F_2^i and F_2^j indicate the perpendicular to the crack plane nodal forces at the tip and at the mid-side node in front of the crack, respectively (Fig. 11). Also, u_2^l, u_2^{l*} and u_2^m, u_2^{m*} represent the opening displacement of the upper and lower crack surfaces at the four nodes placed behind the crack tip and a similar expression for G_{II} [28].

The calculated G_I and G_{II} values approximate the crack-tip energy release rate on the basis of the following assumptions: (i) a crack extension of Δa from $\alpha+\Delta a$ (node i) to $\alpha+2\Delta a$ (node k) does not considerably modify the state at the crack tip, and (ii) the energy released when the crack is extended by Δa from $\alpha+\Delta a$ to $\alpha+2\Delta a$ is equal to the energy required to close the crack between location i and k (Fig. 11) [31]. These two assumptions are considered acceptable for the constitutive material behavior used in the present analysis, resulting in linear elastically-deformed martensitic region surrounding the crack tip [9]. During virtual crack growth under which temperature and tractions at the boundary points are retained constant, it is assumed that most of the dissipation within the cracked body originates from the separation work, i.e., the contribution of the rate of the transformation strain work with respect to crack length, $\partial U^t/\partial a$, in the energy balance equation [9]

$$\frac{\partial W}{\partial a} - \frac{\partial U^e}{\partial a} = C + \frac{\partial U^t}{\partial a}, \quad (43)$$

is small compared to the separation work since the region close to the crack tip is fully transformed. In the above equation, $\partial W/\partial a$ is the work rate supplied by the external loads and $\partial U^e/\partial a$ is the rate of elastic strain energy [9]. Essentially it is assumed that at constant temperature and tractions at the external boundary a differential crack growth results mainly in a stress redistribution in the region of elastically-deformed martensite close to the crack tip [9].

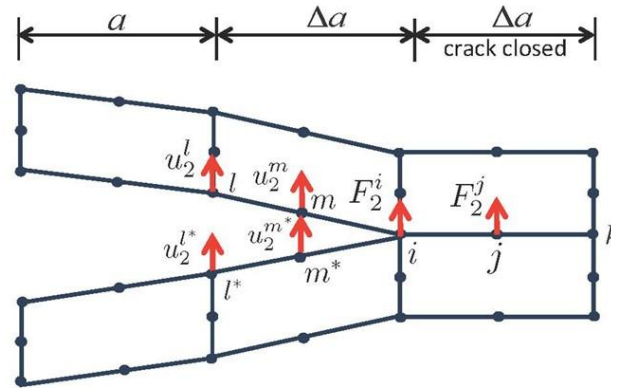


Fig. 11: VCCT for eight-noded elements.

The evolution of the strain energy release rates at the crack-tip under the combined mode I and II conditions are presented for four different ratios r/t_{SMA} : (i) 10, (ii) 40, (iii) 200 and (iv) 400 and for two different initial crack lengths, t_c : 0.05 mm and 0.1 mm as a function of the martensite volume fraction at far field (Figs 12 and 13). As shown in the Figs, for an initial imperfection of length 0.05mm, the critical energy release rate (toughness) of the interface must be less than $41 J/m^2$ in mode I and less than $28 J/m^2$ in mode II for the crack to remain static until the entire SMA-coating reverse transforms back to austenite inducing the required compressive stresses in the aluminum core. In mixed mode fracture, of course, a fracture criterion should be a combination of mode I and mode II energy release rates. There are many such criteria in the literature but only experimental data will allow for choosing the more relevant one for the actual interface toughness response [30, 31]. As expected, the driving force for crack growth increases with increasing crack length and increases with decreasing ratio r/t_{SMA} , which essentially increases the value of the compressive stresses in the core. It should be noted that these values correspond to a rather brittle material such as the interface is expected to be.

5.3 Modelling of the system SMA-coating—Structure

Since SMA coatings on aluminum structural elements are being developed for modular structures made of beams, this section considers the benefits that a SMA coating can induce to the bending response of an aluminum beam.

Thus, a straight beam of length $l=40$ mm and circular cross section is considered as previously (Fig. 14). The beam consists of an aluminum core of radius r and an SMA coating of thickness $t_{SMA}=0.01$ mm. Initially, the SMA coating is at an axially pre-strained martensitic phase while the entire

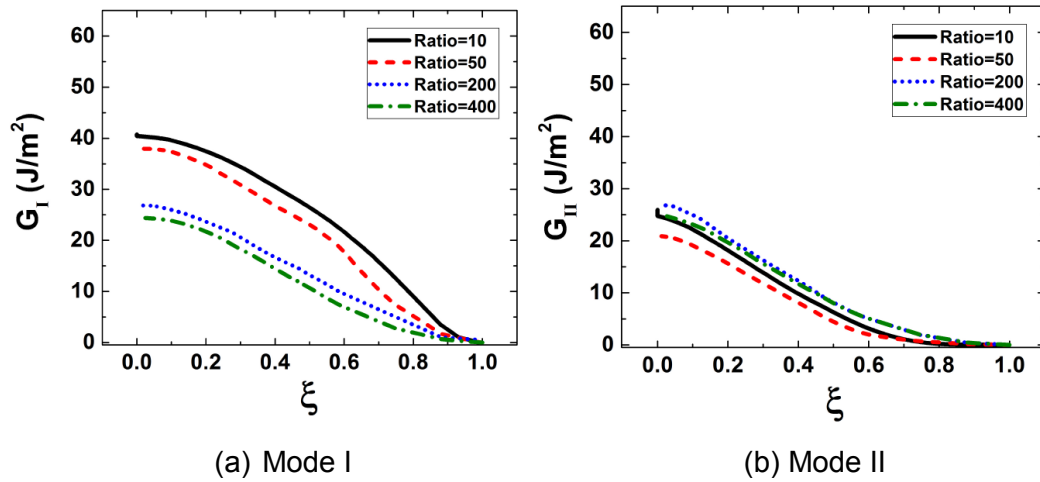


Figure 12: Strain energy release rate for crack length $t_c=0.05$ mm as a function of martensite volume fraction.

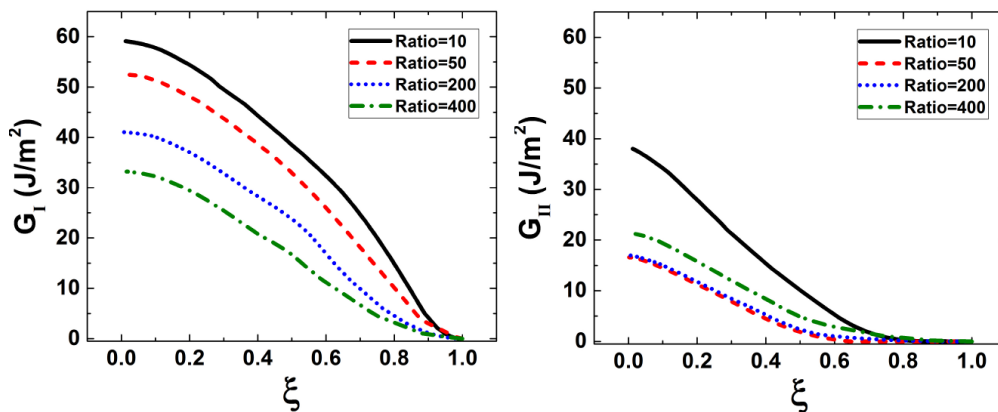


Figure 13: Strain energy release rate for crack length $t_c=0.01$ mm as a function of martensite volume fraction.

structure is under a uniform temperature of 250 K. To investigate the effect of the SMA coating on the response of the structure, three different geometries with ratios r/t_{SMA} : (i) 10, (ii) 40 and (iii) 400 are considered. In each case, the temperature of the structure is increased in order the SMA to return to its austenitic phase and hence introduce compressive stresses to the core as explained in Section 5.1. At that point, a moment, M_y , with magnitude 0.1, 10 and 10000 Nm is applied respectively to the free end of each of the three considered geometries and enforces the structure to bend. The models are developed with the continuum 3D FE (C3D20R) and 3D shell FE (S4R) of ABAQUS FE software.

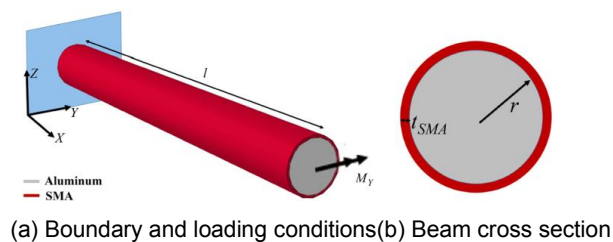


Fig. 14: Aluminum beam with SMA coating.

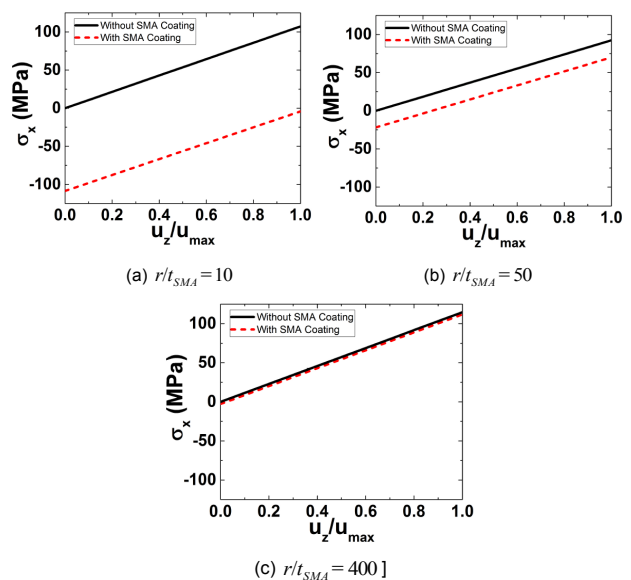


Fig. 15: Maximum tensile stress on the aluminum surface vs normalized deflection for geometries with different r/t_{SMA} ratios.

The maximum stress values on the upper surface of

the aluminum structure, which is under tension upon the application of the moment M_{y_2} are shown in Fig. 15 as a function of normalized deflection for each of the considered ratios r/t_{SMA} . Results for structures with and without SMA coatings are included in order to facilitate conception of the benefits of the SMA coating.

The outcome of the simulations is that the tensile stresses induced in the presence of the SMA coating are reduced by an amount that is approximately equal to the initial compressive stresses throughout the bending loading. These compressive stresses thus contribute to the rigidity and stiffness of the aluminum beam to endure the applied loading conditions in a safe manner and are further expected to enhance the beam's fatigue properties.

As common in SMA research, thermal expansion mismatch effects between the SMA coating and the beam were not included in the analysis because the transformation strains are an order of magnitude larger than the resulting strains and, therefore, the corresponding effect is negligible in the presence of transformation [9, 32].

Contraction of the SMA coating during transformation from oriented martensite to austenite results in tensile stresses in the coating, compressive stresses in the core aluminum material, and no shear stresses at the interface, under the assumption of a perfectly coherent interface. In our finite element calculations, all the shear stresses at the interface remain less than 0.5 MPa throughout the contraction of the SMA coating (Fig. 16). In the presence of an interface imperfection, however, shear stresses develop at the interface and have been taken into account in our analysis presented in Section 5.2 through the measurement of the energy release rate, G_{II} , which is related to mode II loading, i.e., sliding mode (a shear stress acting parallel to the plane of the crack and perpendicular to the crack front). G_{II} raises to relatively high values that always remain less than those of G_I related to mode I. Thus, in conclusion, shear forces at the interface are important only in the presence of a pre-existing crack/imperfection at the interface and are expected to contribute to crack growth, if any, by raising the G_{II} -values. Crack growth is expected to take place whenever the G_I and G_{II} values satisfy a fracture criterion determined from experimental data.

6. MATERIALS AND HEAT TREATMENT

In order to enable the NiTi material to be beneficially used as SMA coating, NiTi alloys of different compositions were considered, as well as the effect

$\sigma_{12} = 0.55$ MPa
 $\sigma_{13} = 0.30$ MPa
 $\sigma_{23} = 0.03$ MPa



Figure 16: State of shear stresses at the SMA coating/substrate interface.

of different microstructures producing precipitates of different sizes. The influence of the composition and precipitates on the thermomechanical properties were also examined.

Two different NiTi compositions considered, each offering both advantages and disadvantages for the chosen application were:

- Equiatomic composition, which is prone to large amount of TRIP since there are no precipitates to stabilize the response and has fixed transformation metrics and high transformation strain [2, 29], and
- Ni-rich Ni50.8Ti (at.%) composition, in which precipitates can be formed by appropriate heat treatment, thereby stabilizing the response of the material against TRIP. Therefore, the Ni-rich composition offers tuneable transformation metrics, adequate resistance to TRIP, but lower transformation strain [2, 29].

During phase transformation there is deformation misfit between the martensitic and austenitic phases present in the material. At that instance, the stress can locally exceed the material's yield strength, leading to local plasticity. By inducing obstacles such as precipitates to the movement of dislocations, one can obtain less TRIP. Therefore precipitates, as non-transforming particles cause transformation strains to decrease (by amounts as per the rule of mixtures) [9].

In the case of NiTi SMA with equiatomic composition, in absence of precipitates, there is more plasticity in the material, but also transformation strains are higher. However, in the case of Ni-rich material, the presence of precipitates causes the plastic deformation to be suppressed [6]. This means that in the case of an application that requires that the SMA material is used in a large number of cycles (e.g. in an actuating device) the composition of choice is Ni-rich. On the other hand, applications requiring the SMA material to be used in a few cycles (e.g. the SMA coating structural application in this study) can use NiTi SMA with equiatomic composition as well as Ni-rich material.

Based on the above argumentation, Ni-rich Ni50.8Ti was selected as the material of choice for the tar-

get coating application of this study, ie aeronautical structural parts anticipated to undergo extensive fatigue cycles. In addition to NiTi composition, the geometry of the aluminum substrate necessary for deposition of the coating plays an important role in an effort that the SMA coating obtains a shape memory effect (Fig. 17). To this regard, a two-phase coating deposition process is being proposed. During Phase 1, the SMA coating is deposited on the compressive side of a bent aluminum substrate. After deposition of the SMA coating, the coating/substrate structure will be left to reach ambient temperature, while the structure remains bent, so that the NiTi coating reaches the martensitic state. Since, at this stage, no stress is applied on the coating, the SMA coating material is self-accommodated martensite – twin structure. This completes Phase 1. During Phase 2, the SMA coating/substrate structure will be unloaded, regaining its original shape. The SMA coating then, will be under tension in a detwinned state. By heating the structure, the SMA coating will transform to austenite, therefore, compressive stresses will be induced in the structure as the SMA coating is trying to change its shape by shrinking.

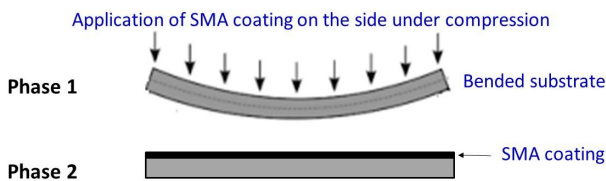


Fig. 17: SMA coating deposition process on an aluminum substrate in order to for the coating to obtain the SME

One of the most important parameters for the coating to obtain a shape memory effect is the appropriate aging heat treatment. NiTi coatings of equiatomic composition require high phase transformation temperatures in order to obtain the shape memory effect. On the other hand, the phase transformation temperature of coatings of Ni-rich composition can be tailored depending on the coatings' microstructure which depends on the precipitates therein. Such tailoring of the phase transformation temperature of Ni-rich coatings can be achieved by heating during Phase 2 of the aforementioned fabrication process. The heating temperature depends on the SMA material composition and microstructure. In equiatomic NiTi material, the austenite appears at a phase transformation temperature of about 107°C. However, for as-received SMAs with Ni-rich composition, in absence of precipitates, the austenitic temperature is 35°C. Precipitate presence in the material's micro-

structure influences the austenitic temperature. For instance, in Ni-rich composition, with incoherent precipitates with the austenite matrix of heterogeneous distribution (with average size of particles about one micrometer), the austenitic temperature is above 35°C, while in Ni-rich composition, where coherent nano-precipitates of homogeneous distribution are formed, the austenitic temperature is below 35°C.

A Thermolab HP1000 hot press was used to perform heat treatments on the SMAs. The system is equipped with furnace, temperature controller and pressure controller and can be programmed to a desired thermal cycle with custom ramp rates for heating as well as cooling. The maximum temperature of the furnace is 1100°C and maximum pressing force is 15000 Kg. The size of the stainless steel vessel of the furnace is 150x200x250 mm and is equipped with ceramic fiber chamber inside. It has a cooling water supply capacity of 1,5 bar and cooling water flow capacity of 3 lt/min. The furnace is capable of performing heat treatments either in air at desired airflows, in vacuum, or in inert atmosphere, such as argon. The specimens were placed in the furnace after the set temperature was reached and where quenched in water at ambient temperature after the end of the heat treatments.

Four different aging heat treatments were considered in this study for processing Ni_{50.8}Ti_{49.2} (at.%) SMA specimens by introduction, in the material bulk, of Ni₄Ti₃ precipitates of different sizes depending on temperature and heating duration.

Fig. 18 presents a schematic of heat treatment 1 (HT1) which consists in heating the material at 500°C for one hour, followed by water quenching (WQ) for cooling. During this heat treatment, isolated incoherent Ni₄Ti₃ precipitates start to form along the grain boundaries.

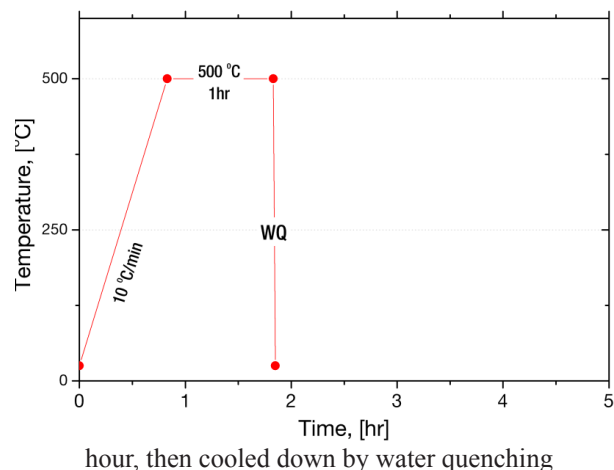


Fig. 19 shows the thermal cycle of heat treatment 2 (HT2) which consists in heating the material at 500°C for 24 hours, followed by water quenching for cooling. During this heat treatment, incoherent precipitates start growing in size and spread homogeneously across the matrix.

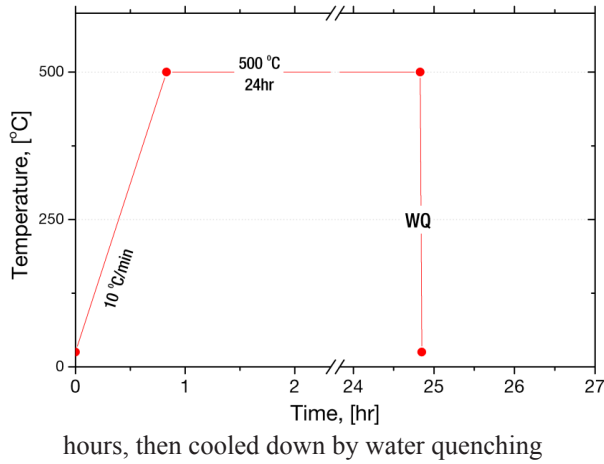


Fig. 20 is the thermal cycle of heat treatment 3 (HT3) which consists in heating the material at 500°C for one hour followed by water quenching, then heating at 300°C for 24 hours and cooled by water quenching. During this heat treatment, coherent nano-precipitates start forming in the matrix and mix with larger in size incoherent precipitates.

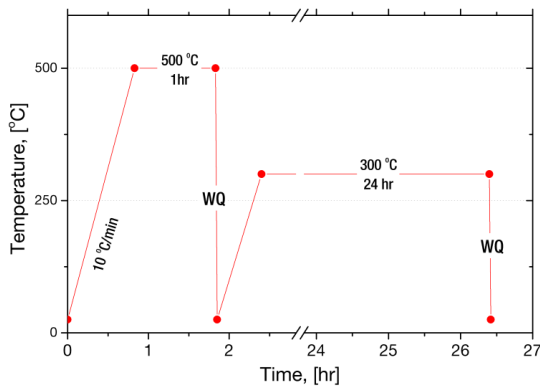


Fig. 20:Heat treatment HT3: Heating at 500°C for one hour followed by water quenching, then heating at 300°C for 24 hours and cooled by water quenching

Fig. 21 depicts the thermal cycle of heat treatment 4 (HT4) which consists in heating the material at 300°C for 100 hours, then cooled by water quenching. During this heat treatment, evenly distributed fine coherent nano-precipitates are forming in the matrix.

Fig. 22 presents TEM (transmission electron microscopy) images of Ni-rich Ni50.8Ti (at.%) SMA after stress-free aging at 500°C for 24 hours. It is

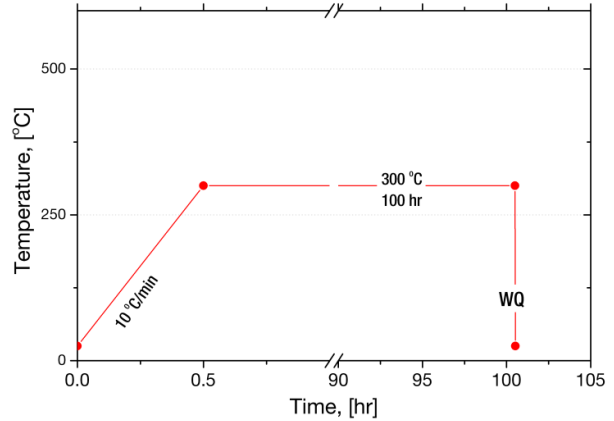


Fig. 21:Heat treatment HT4: Heating at 300°C for 100 hours, then cooled down by water quenching

observed that Ni₄Ti₃ precipitates are incoherent and have rhombohedral atomic structure and lenticular shape [33]. Fig. 23 shows TEM images of Ni-rich Ni50.8Ti (at.%) SMA after stress-free aging at 300°C for 100 hours. During processing, the Ni-rich NiTi SMA material was subjected to the aforementioned aging heat treatment where Ni₄Ti₃ coherent nano-precipitates were formed.

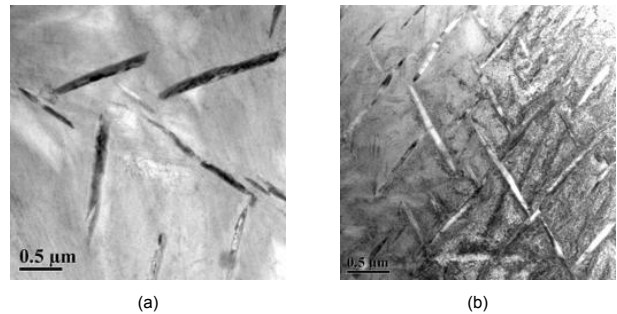


Fig. 22: TEM images of Ni-rich NiTi matrix with Ni₄Ti₃ incoherent precipitates after aging at zero stress at 500°C for 24 hours. The images show formation of diverse crystallographic Ni₄Ti₃ precipitate variants (a) close to and (b) distant from a grain boundary

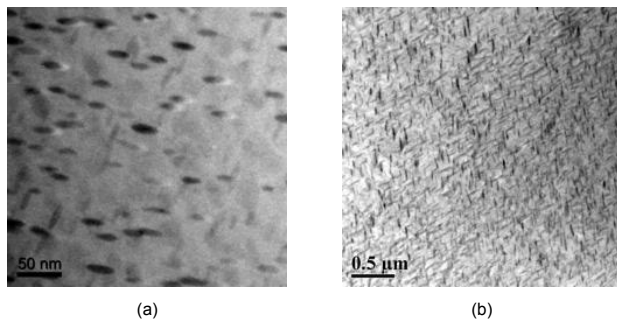


Fig. 23: TEM images at different scales of Ni-rich NiTi matrix with Ni₄Ti₃ coherent nano-precipitates after aging at zero stress at 300°C for 100 hours

7. ASSESSMENT OF THE OBTAINED SHAPE MEMORY EFFECT OF THE NITISMA COATINGS

The transformation from austenitic to martensitic phase, and the reverse transformation, are associated with latent heat absorption and release. To determine the transformation heat and the related transformation temperatures of the SMA, thermal analysis used to determine phase transformation temperatures of materials, latent heat aroused from transformation, as well as the specific heat capacity of the material, necessitating tiny quantities of the material [21,34,35].

Fig. 24 summarizes the peak temperatures of equiatomic and Ni-rich Ni_{50.8}Ti_{49.2} SMA in the four different heat treatments, HT1-HT4, for increasing aging temperature and time. The elevated transformation temperatures are observed for the aging heat treatment with the highest temperature/time, which is comparable to the peak temperatures of the equiatomic composition. By examination of the data, the optimum aging heat treatment for Ni_{50.8}Ti_{49.2} for using the material in SMA coating form can be clearly identified as HT4.

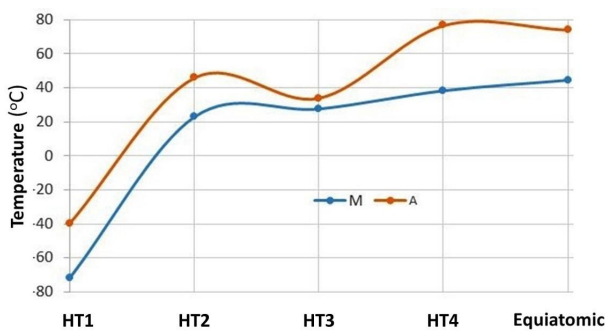


Fig. 24: Comparison diagram for the peak transformation temperatures of Ni_{50.8}Ti_{49.2} in four different aging heat treatments and of equiatomic NiTi SMA.

8. ASSESSMENT OF THERMO-MECHANICAL FATIGUE OF NITI SMAs

In view of the potential target application for the developed SMA coatings in the conventional aircraft wing box and fuselage structures for the enhancement of structural integrity of aeronautical structures, investigation of the thermo-mechanical fatigue response of the material and the influence of heat treatment conditions, therein, appears indispensable. Dog-bone shaped NiTi specimens for characterization of actuation fatigue were fabricated using electro-discharge machining (EDM) from 0.5 millimeter-thick NiTi sheet material (Fig. 25). Samples with cross-section of 3.125 mm by 0.50 mm were tested. A wet grinding wheel was used to grind and polish the specimens after EDM, initially using a 400 grit grinding paper, next a 1200 grit, finally a 2000 grit. After grinding, the specimens

were polished with a polishing disk and appropriate aluminum oxide particle suspensions, namely 5µm particles initially followed by 0.3µm particles, for approximately 4 minutes per suspension. At the end, all samples had mirror-finishes on their sides.

Ni-rich Ni_{50.8}Ti_{49.2} (at.%) SMA was used with adjustable transformation temperatures by means of different heat treatments.

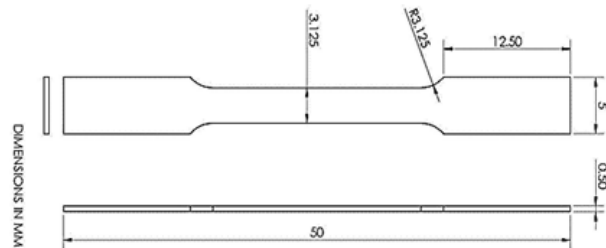


Fig. 25: Specimen geometry

Ni_{50.8}Ti_{49.2} (at.%) SMA specimens were loaded on an electro-mechanical testing system Instron 5960 (Fig. 26a). The samples were heated resistively (Joule heating) and cooled by forced air convection so that complete transformation was attained during each cycle. All samples were cycled to failure. IR thermography (CEDIP JADE IRT system) was used to ensure that consistent cycling conditions were maintained (Fig. 26b).

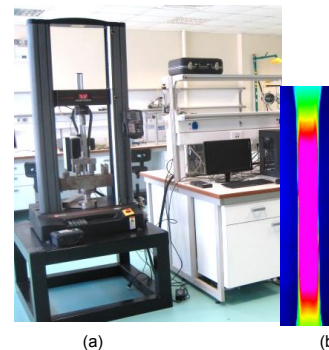


Fig. 26: (a) Mechanical testing system; (b) IR thermogram measuring temperature on the specimen during actuation cycling

All transformation-induced fatigue tests were performed at a constant stress level of 200 MPa. Samples were cooled below the martensitic finish temperature and, because of the applied load, underwent twinning, simulating the SMA coating application on a bending NiTi specimen. Next, thermal cycling was imposed on the specimens until their failure. As it was not possible to mount thermocouples on a sample during the tests, measurements using LVDT displacement were employed to make sure that there was full actuation during the thermal cycling. The tests were conducted in time-controlled cycles,

while setting the time amount for cooling and heating. It was observed that about three seconds of heating were necessary to carry the specimens above Af temperature, under application of current of 2.5 V and 20 A. In addition, about ten seconds were necessary for cooling the samples below Mf temperature. Therefore, a total actuation cycle was completed in approximately 13 seconds. As heating was performed by Joule heating, passing current through the specimen and not by a furnace, and the sample was cooled by forced air convection, there were no specific experimental temperatures set. It was made sure that temperature exceeded Af and fell below Mf at each actuation cycle, since this was the main objective in actuation fatigue.

Two displacement data-points were collected in every thermal cycle (Fig. 27): the first, in the austenitic phase (at the end of heating) and the second in the martensitic phase (at the end of cooling). This was done at each cycle during the actuation fatigue test. The strains were subsequently calculated from the displacements (measured by LVTD) and plotted versus the thermal cycles (Fig. 28). When an SMA specimen recovers repeatedly the strain via the SME, the material will be subjected to actuation fatigue and will produce irrecoverable deformation [36]. The strain in the martensite represents the total strain (i.e. thermal + actuation + irrecoverable) and the strain in the austenite is related to the irrecoverable strain. The actuation strain for every cycle is the difference between the martensitic and austenitic strains [37].

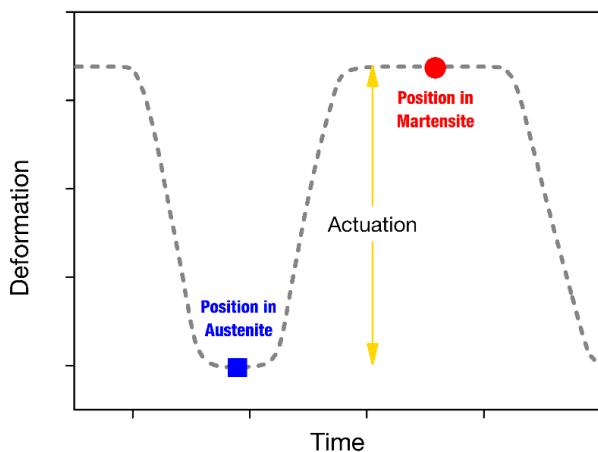


Fig. 27: Displacement /time plot with the data acquisition points

The results on actuation fatigue are expressed in the form of three curves representing the strain in the martensitic phase, the strain in the austenitic phase, and the actuation strain.

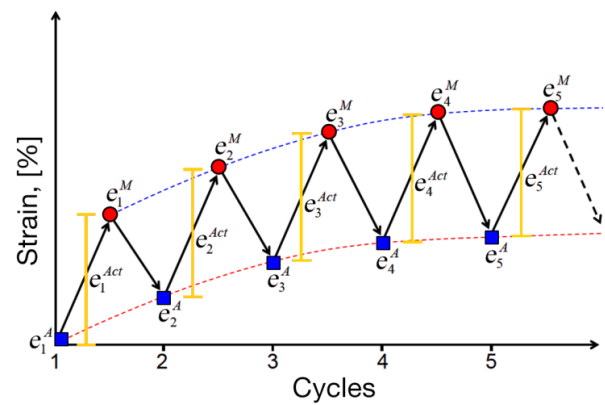


Fig. 28: Strains for each cycle in the martensitic and austenitic phases versus thermal cycles

Actuation fatigue was performed to $\text{Ni}_{50.8}\text{Ti}_{49.2}$ SMA specimens subjected to appropriate heat treatments in order to verify the SME effect of the materials. This will be a driver for proper aging heat treatment of the SMA NiTi coatings with same element composition. Processing the Ni-rich NiTi SMAs, such as $\text{Ni}_{50.8}\text{Ti}_{49.2}$, has an objective to form Ni-rich precipitates, such as Ni_4Ti_3 precipitates, to stabilize thermal cyclic response of the material. The process is similar to precipitation hardening in non-SMA metallic alloys.

The SMA specimens were subjected to actuation fatigue under isobaric mechanical loading at a stress level of 200 MPa, Joule resistive heating and convective cooling. The evolution of the strains in the austenite, in the martensite, as well as the actuation strain, were plotted through the life of the specimens.

Fig. 29 presents the % strain in austenite, in martensite, and actuation as function of cycles until failure of $\text{Ni}_{50.8}\text{Ti}_{49.2}$ SMA at the as received (as rolled) condition. We observe a limited fatigue life below 600 cycles, an unstable actuation response between 0.12% and 0.31% and limited irrecoverable stain of 0.5% at failure.

Fig. 30 shows the evolution of the strains for a $\text{Ni}_{50.8}\text{Ti}_{49.2}$ specimen that underwent a heat treatment at 500°C for 1 hour (HT1). At this aging heat treatment, the SMA material developed only small amount of incoherent Ni_4Ti_3 precipitates. This sample failed after only 532 cycles. The actuation strain, however, was constant at 1.2%, and the total irrecoverable strain at failure was 2.2%.

Fig. 31 presents the strain evolution for a $\text{Ni}_{50.8}\text{Ti}_{49.2}$ specimen that underwent heat treatment at 500°C for 24 hours (HT2). At this aging heat treatment, the SMA material formed incoherent Ni_4Ti_3 precipi-

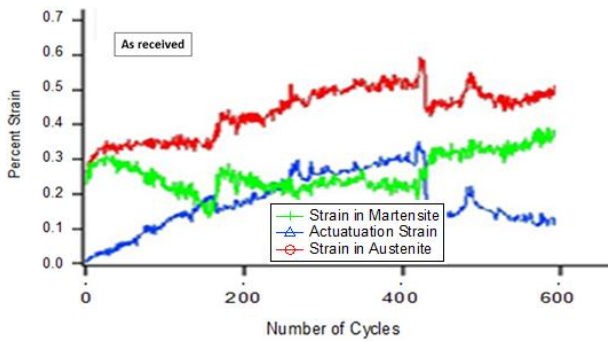


Fig. 29: Strain evolution showing the strain in the martensite, the strain in the austenite, and the actuation strain for as received $\text{Ni}_{50.8}\text{Ti}_{49.2}$ SMAs

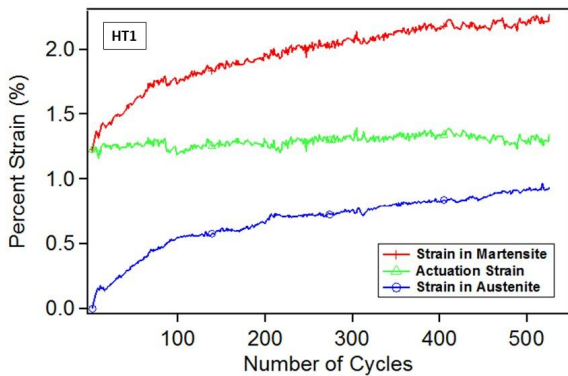


Fig. 30: Strain evolution showing the strain in the martensite, the strain in the austenite, and the actuation strain for aging heat-treated $\text{Ni}_{50.8}\text{Ti}_{49.2}$ SMAs in HT1 conditions.

tates. This sample failed after 2540 cycles. The actuation strain was constant at 1.52%, and the total irrecoverable strain at failure was 1.05%

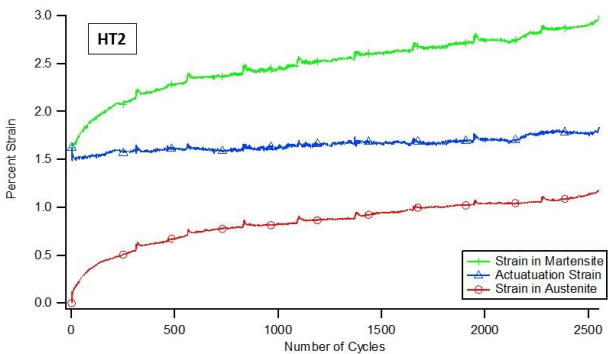


Fig. 31: Strain evolution showing the strain in the martensite, the strain in the austenite, and the actuation strain for aging heat-treated $\text{Ni}_{50.8}\text{Ti}_{49.2}$ SMAs in HT2 conditions

Fig. 32 presents the strain evolution for a $\text{Ni}_{50.8}\text{Ti}_{49.2}$ specimen that underwent heat treatment at 300°C for 100 hours (HT4). At this aging heat treatment, the SMA material formed coherent Ni_4Ti_3 nano-precipitates. This sample failed after 2728 cycles. The

actuation strain was constant throughout the test at 1.3%, and the total irrecoverable strain accumulated slowly and at failure was 2.02%.

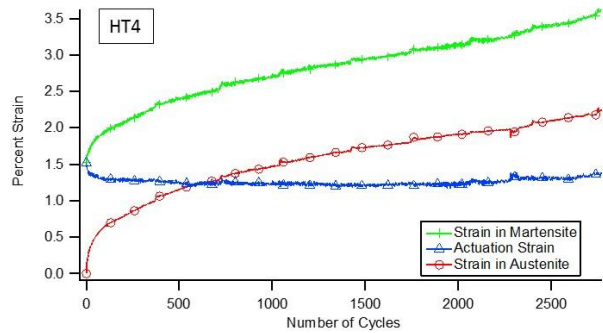


Fig. 32: Strain evolution showing the strain in the martensite, the strain in the austenite, and the actuation strain for aging heat-treated $\text{Ni}_{50.8}\text{Ti}_{49.2}$ SMAs in HT4 conditions

Fig. 33 presents the strain evolution for a $\text{Ni}_{50.8}\text{Ti}_{49.2}$ specimen that underwent heat treatment at a much higher temperature of 800°C for 1 hour. At this aging heat treatment, the SMA material failed after only 210 cycles. The actuation behavior of the material showed instability.

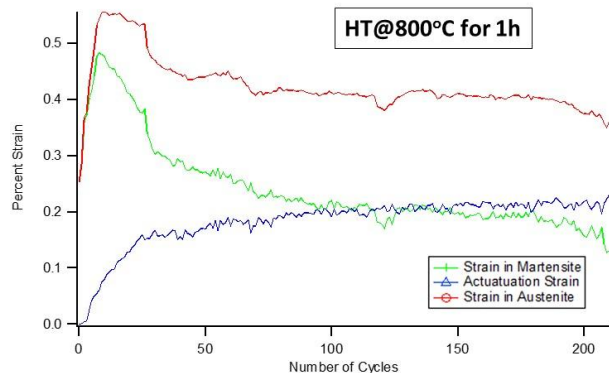


Fig. 33: Strain evolution showing the strain in the martensite, the strain in the austenite, and the actuation strain for aging heat-treated $\text{Ni}_{50.8}\text{Ti}_{49.2}$ SMAs at 800°C for one hour

Finally, Fig. 34 shows the strain evolution for an equiatomic $\text{Ni}_{50.0}\text{Ti}_{50.0}$ (%at.) specimen. The irrecoverable strain is accumulated during the first few cycles. After that, the accumulated irrecoverable strain per cycle stabilizes and very little accumulation occurs until the sample's failure. It was observed that the life of equiatomic NiTi SMA specimen was very low. In addition, the actuation behavior of the material exhibited instability. The actuation strain dropped with the increase of irrecoverable strain,

which is about 8% at the failure point.

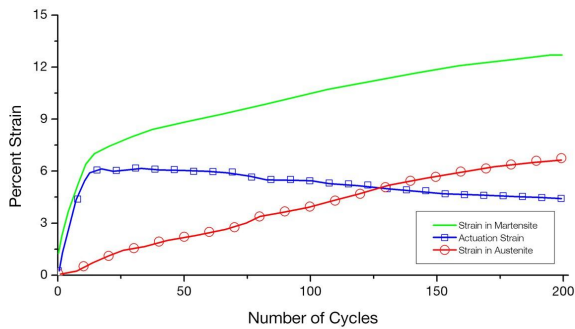


Fig. 34: Strain evolution showing the strain in the martensite, the strain in the austenite, and the actuation strain for equiatomic $\text{Ni}_{50.0}\text{Ti}_{50.0}$ SMAs

9. DISCUSSION AND CONCLUSIONS

The present paper describes the development, for the first time, of SMA coatings on structural elements, for modular structures made of aluminum beams for aerospace applications, such as the conventional aircraft wing box and fuselage structures. The SMA coating applications considered here entail, long aluminum prisms with its lateral surfaces encased in SMA coating.

To demonstrate the beneficial effect of SMA coating on the mechanical response of aluminum beams, a constitutive model for polycrystalline SMAs, implemented in the ABAQUS suite via a user subroutine, was used to analyze the SMA coating–aluminum beam. The model and its implementation were described and its capability in simulating the phenomenology of the SMA response was shown from the comparison of simulations against experimental data obtained from isothermal and isobaric experiments. The thermal expansion mismatch between the SMA coating and the aluminum beam was omitted in the analysis as negligible in the presence of phase transformation as transformation strains were an order of magnitude larger than the resulting strains.

The analysis of the SMA coating–aluminum beam assumes long prisms with variable ratios of SMA thickness to smallest dimension of the beam. According to the modelling results:

- When the SMA coating is initially in the austenitic state and deformed together with the aluminum beam upon uniaxial tensile loading, the required stress levels for sufficient phase transformation to take place is too high for practical applications. The reason being that the transformation strains should be matched by elastic straining of the elastic structure. This loading path is thus not considered of value for the mechanical performance of the elastic

structure;

- The proposed loading path that can induce beneficial compressive stresses upon heating in the aluminum beam requires the SMA coating to be in a detwinned martensitic state when the whole structure, i.e., SMA coating–beam is under zero load; the SMA-coating should be initially oriented martensite with a deformation that can be recovered upon heating and transformation to austenite;

- During the proposed loading, the driving force for decohesion from small initial imperfections takes values that can be withstood from rather brittle materials. However, depending on the toughness of the interface, these results just yield the likeliness of the interface to remain intact during phase transformation. It should also be noted that this loading path yields a negligible stable crack growth regime.

The behavior of the SMA coating/substrate interface was assessed using VCCT approach yielding a single value for the driving force for crack growth, which is the energy release rate, hence providing a straightforward approximation of the required interface toughness for structural integrity. VCCT presents considerable advantage over cohesive elements, which require at least two parameters to define the cohesive-traction separation law for each fracture mode (instead of one for VCCT), and the choice of these has a great influence on the toughness response of the structure.

- For the proposed loading path,
 - the ratio between the thickness and the smallest dimension of the aluminum beam is crucial for the levels of compressive stresses that can be developed in the beam once the SMA coating is transformed from oriented martensite to austenite recovering its initial deformation. This result can be understood within a rule of mixture context;

- contraction of the SMA coating during transformation from oriented martensite to austenite results in tensile stresses in the coating that increase the temperature raise required for full transformation. The levels of stress and consequently the temperature raise required for full transformation may take non-permissible values. However, no full transformation is required if the compressive stresses developed in the aluminum during partial transformation take desirable values;

- A proposed fabrication method that will result in initially deformed SMA-coating may be deposition on the compressive side of the aluminum beam when under bending at low temperatures. Load removal will create tensile stresses and detwinning on the SMA-coating resulting in oriented martensite

and macroscopic deformation.

- SMA-coating–aluminum beam simulations were performed under bending to depict the beneficial effect of the initial compressive stresses induced in the aluminum beam on its surface that is under tension during bending. The outcome of the simulations is that the tensile stresses induced in the presence of the SMA coating are reduced by an amount that is approximately equal to the initial compressive stresses. Thus, the induced compressive stresses contribute to the rigidity and the stiffness of the aluminum beam to endure the applied loads in a safe manner and are further expected to enhance their fatigue properties.
- Since the shear stresses at the interface remain less than 0.5 MPa throughout the contraction of the SMA coating, shear forces at the interface are important only in the presence of a preexisting crack/imperfection at the interface and are expected to contribute to crack growth.

Martensitic transformation determines all critical properties of SMAs, including superelasticity and SME. The final transformation temperature is considered as one of the most significant material properties in NiTi SMAs, since it governs the transition between superelastic and shape memory behavior. The transformation temperature in SMAs can be controlled by choosing proper alloy composition and appropriate aging heat treatment, which modifies the microstructure by introducing precipitates. Even short-time heat treatments at moderate temperatures can influence the mechanical properties and transformation behavior of SMAs.

For specific SMA applications, such as actuators, cyclic training is required in order for the material to stabilize its response and memorize high and low temperature shapes without any applied force. For structural applications, however, such as SMA coating deposited on metallic substrates, no SMA training is required. This is because the SMA has to contribute to the stiffness and rigidity of the structure to safely withstand the expected loads, as well as to possess improved fatigue behavior by inducing to the beam compressive stresses through its single-time activation at an appropriate temperature.

NiTi coatings were considered in two different compositions: (a) equiatomic, which is prone to TRIP, since there are no precipitates, and has a fixed transformation metrics and high transformation strain, and (b) Ni-rich Ni_{50.8}Ti (at.%), where precipitates can be formed by appropriate heat treatment, thereby stabilizing the material's response against TRIP. Hence, Ni-rich composition is preferable since it offers tunable transformation metrics, adequate resis-

tance to TRIP, but lower transformation strain.

For using SMA materials in actuating devices, requiring the SMA to be operated in a large number of cycles, the material composition of choice would be Ni-rich. However, for an application, such as SMA coating for structural components, which require the SMA to be used in a few cycles, both Ni-rich and equiatomic NiTi can be utilized. It was, therefore, decided that while Ni-rich would be the material of choice for coating application, equiatomic NiTi remains an option as an alternative material, in case that the Ni-rich material fails to achieve its objectives.

For the SMA coating to exhibit shape memory effect, the coating should to be subjected to appropriate processing conditions and be deposited on a metallic substrate with proper geometry according to newly suggested two-phase coating deposition process is involving deposition of the coating on the compressive side of a bent aluminum substrate beam. At the final stage, heating the structure will lead the SMA coating to transform to austenite, inducing compressive stresses as the SMA coating is trying to change its shape by shrinking.

Appropriate aging heat treatment was identified as of paramount importance for the coating to exhibit the shape memory effect. Ni-rich Ni_{50.8}Ti (at.%) SMAs, after stress-free aging at 500°C for 24 hours, lead to the formation of Ni₄Ti₃ incoherent precipitates, while by subjecting the material to aging at 300°C for 100 hours, there is formation of Ni₄Ti₃ coherent nano-precipitates. This fact directly influences the SMA coating transformation temperature, where in the first case it is above 35°C, while at the latter case the austenitic temperature is lowered below 35°C.

It was found that heat treatment conditions also had an important effect on thermo-mechanical fatigue response of the material. With the increase of heat treatment temperature and time, NiTi SMAs exhibited more ductility and could handle more irrecoverable strain before failure. It was found that heat treatments of 300°C for 100 hours (termed HT4) produced SMAs with the longest fatigue lives, because, due to the formation of coherent nano-precipitates, they represent a combination of both the capability to endure large amount of irrecoverable strains, as well as the ability to exhibit stable actuation strains, unlike samples with higher heat treatment temperature which showed localized strains and poor actuation fatigue response. This is also in agreement with the results of thermal analysis, where the specimens with HT4 proved to be an optimum aging heat treatment for Ni_{50.8}Ti_{49.2} SMA that is suitable to be used

for developing SMA coatings.

It was found that during actuation fatigue testing of $\text{Ni}_{50.8}\text{Ti}_{49.2}$ SMAs at various heat treatments, actuation strain remained constant throughout the life of the samples for heat treatments promoting the formation of Ni_4Ti_3 precipitates. It can be concluded that $\text{Ni}_{50.8}\text{Ti}_{49.2}$ SMAs form precipitates in its matrix that can enhance the material properties, including to stabilize the actuation strain and limit plastic strain accumulation.

However, constant stability of actuation strain, without necessitating general training, is not a characteristic of equiatomic NiTi SMAs. This also is in accordance to findings in the literature [38]. While precipitation hardening clearly affects the SMA material's performance, since actuation strain remains constant from start to end of the test, and the irrecoverable strains are limited to less than 3%, equiatomic NiTi SMAs, which do not promote formation of precipitates, attain irrecoverable strains of 8%. In addition, as irrecoverable strain raises over cycling, the correspondent actuation strain declines. This is where the formation of precipitates proves its importance for SMA materials. The actuation strains are not reduced as irrecoverable strains accumulate in Ni-rich NiTi SMAs, and the build-up of irrecoverable strains is limited to a lesser amount.

ACKNOWLEDGEMENT

This work was supported by the European Commission under "Horizon 2020 – The Framework Programme for Research and Innovation (2014-2020): Future and Emerging Technologies (FET Open)", project title: "An Innovative Method for Improving the Structural Integrity using SMA Revolutionary Technology – InnoSMART" (Project reference number: 664892).

REFERENCES:

- [1] K. Otsuka, C.M. Wayman (Eds.), *Shape Memory Materials*, Cambridge University Press, Cambridge, 1999.
- [2] D.C. Lagoudas(Ed.), *Shape Memory Alloys: Modeling and Engineering Applications*, Springer, New York, 2008.
- [3] D.C. Lagoudas, P.B. Entchev, P. Popov, E. Patoor, L.C. Brinson, and X. Gao, *Shape memory alloys. Part II: Modeling of polycrystals*, *Mech. Mater.* 38, (2006) 430–462.
- [4] E. Patoor, D.C. Lagoudas, P. B. Entchev, L.C. Brinson, X. Gao, *Shape memory alloys. General properties and modeling of single crystals*, *Mech. Mater.* 38, (2006) 391–429.
- [5] J. Frenzel, A. Wiecek, I. Opahle, B. Maaß, R. Drautz, G. Eggeler, *On the effect of alloy composition on martensite start temperatures and latent heats in Ni–Ti-based shape memory alloys*, *ActaMaterialia* 90 (2015) 213–231.
- [6] T. Baxevanis, D.C. Lagoudas, *Fracture mechanics of shape memory alloys: review and perspectives*, *Int. J. Fract.* 191 (2015) 191–213.
- [7] A.R. Pelton, J. DiCello, S. Miyazaki, *Optimisation of processing and properties of medical grade nitinol wire*, *Min. Invas. Ther. Allied Tech.*9(2) (2000) 107–118.
- [8] J. Boyd, D.C. Lagoudas, *Athermodynamical constitutive model for shape memory materials. The monolithic shape memory alloy*, *Int. J. Plast.* 12 (1996) 805–842.
- [9] T. Baxevanis, A.F. Parrinello, D.C. Lagoudas, *On the driving force for crackgrowth during thermal actuation of shape memory alloys*, *J. Mech. and Phys. of Solids* 89 (2016) 255–271.
- [10] T. Duerig, K. Melton, D. Stockel, C. Wayman (Eds.), *Engineering Aspects of Shape Memory Alloys*, Butterworth-Heinemann, London, 1990.
- [11] K. Otsuka, C. M. Wayman (Eds.), *Shape Memory Materials*, Cambridge University Press, Cambridge, 1999.
- [12] P. Kumar, D.C. Lagoudas, and D. Lagoudas, *Shape Memory Alloys - Modelling and Engineering Applications*, Springer Science, New York, NY, 2008.
- [13] T. Ezaz, J. Wang, H. Sehitoglu, H.J. Maier, *Plastic deformation of NiTi shape memory alloys*", *ActaMaterialia* 61(1) (2013) 67-78.
- [14] R. Mirzaeifar, R. DesRoches, A. Yavari, K. Gall, *A micromechanical analysis of the coupled thermomechanical superelastic response of textured and untextured polycrystalline NiTi shape memory alloys*, *ActaMaterialia*61 (2013) 4542-4558.
- [15] L. Zhao, et al., *The study of niobium-rich precipitates in a Ni TiNb shape memory alloy*.*ScriptaMetallurgicaetMaterialia*24(2) (1990) 221-225.
- [16] J.A. Shaw and S. Kyriakides, *Thermomechanical aspects of NiTi*. *Journal of the Mechanics and Physics of Solids*43(8) (1995) 1243-1281.
- [17] K. Melton, O. Mercier, *Deformation behavior of NiTi-based alloys*, *Metallic Tras.* 9A (1978) 1487–1488.
- [18] W.-S. Ko, S.B. Maisel, B. Grabowski, J. Bae Jeon, J. Neugebauer, *Atomic scale processes of phase transformations in nanocrystalline NiTi shape-memory alloys*, *ActaMaterialia* 123 (2017) 90-101.
- [19] Y.F. Zheng, et al., *Effect of ageing treatment on the transformation behavior of Ti-50.9 at.% Ni alloy*, *ActaMaterialia*56(4) (2008) 736-745.
- [20] M.C. Carroll, J. Michutta, A. Yawny, C. Somsen, K. Neuking, G. Eggeler, *Martensitic phase transformation in Ni-rich NiTi single crystals with one family of Ni₄Ti₃ Precipitates* *A378* (2004) 152-156.
- [21] M. Nishida, C.M. Wayman, R. Kainuma, T. Honma, *Further electron microscopy studies of the Ti11 Ni14*

- phase in an aged Ti-52at%Ni shape memory alloy, *Scr. Metall.* 20 (1986) 899-904.
- [22] M.G. Bignon, M. Morin, Thermomechanical study of the stress assisted two way memory effect fatigue in TiNi and CuZnAl wires, *Scripta Mater.* 35(12) (1996) 1373-1378.
- [23] D. Lagoudas, D. Miller, L. Rong, P. Kumar, Thermo-mechanical fatigue of shape memory alloys, *Smart Mater. Struct.* 18 (2009) 1-12.
- [24] O. Bertacchini, D. Lagoudas, E. Patoor, Thermomechanical transformation fatigue of TiNiCu SMA actuators under a corrosive environment-part I: Experimental results, *Int. J. Fatigue* 31 (2009) 1571-1578.
- [25] S. Jape, T. Baxevanis, D.C. Lagoudas, Stable crack growth during thermal actuation of shape memory alloys, *Shape Memory and Superelasticity* 2(1) (2016) 104-113.
- [26] T. Baxevanis, A.F. Parrinello, D.C. Lagoudas, On the fracture toughness enhancement due to stress-induced transformation in shape memory alloys, *Int. J. Plast.* 50 (2013) 158-169.
- [27] J. Jape, A. Parrinello, T. Baxevanis, D.C. Lagoudas, Chapter 17 - On the fracture response of shape memory alloy actuators, Springer Nature, 2015.
- [28] S. Jape, A. Parrinello, T. Baxevanis, D.C. Lagoudas, On the fracture response of shape memory alloy actuators, *Proc. of TMS Middle East - Mediterranean Materials Congress on Energy and Infrastructure Systems (MEMA)*, 2015, pp. 165-180.
- [29] D.C. Lagoudas, Y. Chemiskya, L. Machado, P. Popov, Constitutive model for the numerical analysis of phase transformation in polycrystalline shape memory alloys, *Int. J. of Plasticity* 32-33 (2012) 155-183.
- [30] Y. Freed, L. Banks-Sills, Crack growth resistance of shape memory alloys by means of cohesive zone model, *J. Mech. Phys. Solids* 55 (2007) 2157-2180.
- [31] S. Jape, A. Solomou, T. Baxevanis, D.C. Lagoudas, Fracture toughness of shape memory alloy actuators: effect of transformation-induced plasticity, *Proc. SPIE, Behavior and Mechanics of Multifunctional Materials and Composites*, 98000C, 2016.
- [32] W. Zaki, Z. Moumni, A three-dimensional model of the thermomechanical behavior of shape memory alloys, *Journal of the Mechanics and Physics of Solids* 55(11) (2007) 2455-2490.
- [33] T. Saburi, NiTi shape memory alloys, In *Shape Memory Materials* (K. Otsuka, C.M. Wayman, Eds.), Cambridge University Press, Cambridge, 1998.
- [34] M. Nishida, T. Honma, All-round shape memory effect in Ni-rich Ti-Ni alloy generated by constrained aging, *Scr. Metall.* 18 (1984) 1293-1298.
- [35] C.M. Wayman, T. Honma, M. Nishida, Precipitation processes in near-equiatomic TiNi shape memory alloys, *Metallurgical Transactions A* 17A (1986) 1505-1515.
- [36] J.L. McNichols, P.C. Brookes, NiTi Fatigue Behavior, *J. Appl. Phys.* 52(12) (1981) 7442-7444.
- [37] B.O. Agboola, D.J. Hartl, D.C. Lagoudas, A study of actuation fatigue of shape memory alloy, *ASME Conf. on Smart Materials, Adaptive Structures and Intelligent Systems*, American Society of Mechanical Engineers, 2012, pp. 287-293.
- [38] J.H. Mabe, R. Ruggeri, F.T. Calkins, Characterization of Nickel-rich Nitinol alloys for actuator development, in: *International Conference on Shape Memory and Superelastic Technologies*, Pacific Grove, CA, 2006.